

Investigating and monitoring central nave vaults of the Turin Cathedral with Acoustic Emissions and Thrust Network Analysis

*Original*

Investigating and monitoring central nave vaults of the Turin Cathedral with Acoustic Emissions and Thrust Network Analysis / Manuello, A.; Marmo, F.; Melchiorre, J.. - In: DEVELOPMENTS IN THE BUILT ENVIRONMENT. - ISSN 2666-1659. - 18:(2024), pp. 1-20. [10.1016/j.dibe.2024.100434]

*Availability:*

This version is available at: 11583/2987825 since: 2024-04-15T09:12:31Z

*Publisher:*

Elsevier

*Published*

DOI:10.1016/j.dibe.2024.100434

*Terms of use:*

This article is made available under terms and conditions as specified in the corresponding bibliographic description in the repository

*Publisher copyright*

(Article begins on next page)



# Investigating and monitoring central nave vaults of the Turin Cathedral with Acoustic Emissions and Thrust Network Analysis

Amedeo Manuella<sup>a</sup>, Francesco Marmo<sup>b</sup>, Jonathan Melchiorre<sup>a,\*</sup>

<sup>a</sup> Politecnico di Torino, DISEG, Department of Structural, Geotechnical and Building Engineering, Corso Duca Degli Abruzzi, 24, Turin, 10129, Italy

<sup>b</sup> Department of Structures for Engineering and Architecture, Università Degli Studi di Napoli Federico II, Via Claudio, 21, Napoli, 80138, Italy

## ARTICLE INFO

### Keywords:

Acoustic emission  
Thrust network analysis  
Masonry vaults  
Historical buildings  
Structural monitoring  
Damage evolution

## ABSTRACT

Ancient masonry constructions and historical buildings, such as cathedrals, are exposed to considerable risks attributed to factors like ageing and long-term exposure to both dynamic and static variations in loading conditions. In this study, an innovative and promising monitoring approach was applied to assess the structural integrity of the vault in the central nave of the Turin Cathedral. Specifically, the outcomes obtained from Acoustic Emissions (AE) are correlated with the insights derived from the Thrust Network Analysis (TNA) conducted on the structure. This analysis considers the structural elements introduced early in the twentieth century to mitigate horizontal forces. Acoustic Emission (AE) is a commonly employed technique in structural monitoring to detect and analyze elastic waves generated by crack formation, providing valuable information about structural damage. The Thrust Network Analysis (TNA) is an approach that applies Heyman's principles to represent stress in masonry vaults. This method models the stresses as a discrete network of forces, achieving equilibrium with gravitational loads. In this context, the results obtained by TNA analysis are strictly correlated with AE localization results.

## 1. Introduction

Historical buildings often exhibit pervasive crack patterns resulting from the simultaneous influence of various conditions on the load-bearing elements, such as static and dynamic loading, temperature variation, subsidence, fatigue, and creep. Non-destructive methods provide a means to evaluate the condition of these structures and their evolution in time (Aggelis et al., 2013; Aki, 1981; Bak and Tang, 1989; Ohtsu et al., 1998; Bak et al., 2002). During the last few years, several studies have employed a monitoring approach based on the spontaneous emission of elastic waves (Melchiorre et al., 2023a) in historical masonry buildings (Anzani et al., 2008; Carpinteri et al., 2016; Lacidogna et al., 2015). By AE monitoring (Scruby, 1987), the signals, emitted by micro-cracks (100–350 kHz), are acquired by wide-band piezoelectric (PZT) sensors and successively post-processed by statistical and analytical analysis (Niccolini et al., 2009). By utilizing the Acoustic Emission (AE) technique, the authors have gained significant expertise in monitoring historical structures, including tall masonry towers (Carpinteri et al., 2013a), monuments with load-bearing walls constructed from stones, and sack masonry systems (Anzani et al., 2008; Lacidogna et al., 2015). The AE technique was employed for controlling

the evolution of structural damage caused by pre-seismic and earthquake activity like in the case of the monitoring of the vertical bearing structure of the Syracuse cathedral (Niccolini et al., 2011a). Moreover, the Acoustic Emission (AE) signals were also employed to provide an interpretation of the impact of repetitive phenomena, such as vehicle traffic and wind effects. As in the case of Asinelli's Tower in Bologna, Central Italy (Carpinteri et al., 2016; Lacidogna et al., 2015). In the current study, the initial analysis focused on the outcomes of Acoustic Emission (AE) monitoring conducted on the vault of the central nave of the Turin Cathedral. The progression of damage is defined through an analysis of the cumulative number of Acoustic Emission (AE) events and various parameters capable of predicting the time-dependent behaviour of damage. More specifically, the b-value analysis indicates a decreasing trend, reaching values consistent with the formation of localized cracks in the section of the monitored structure near specific positions identified in the 3D model of the vault. These findings, coupled with evidence from other AE parameters, are correlated with numerical results obtained through the Thrust Network Analysis (TNA). This analysis considers additional elements introduced at the beginning of the 20th century to mitigate horizontal forces.

Thrust Network Analysis (TNA) is an approach that applies

\* Corresponding author.

E-mail address: [jonathan.melchiorre@polito.it](mailto:jonathan.melchiorre@polito.it) (J. Melchiorre).

<https://doi.org/10.1016/j.dibe.2024.100434>

Received 23 December 2023; Received in revised form 1 April 2024; Accepted 4 April 2024

Available online 6 April 2024

2666-1659/© 2024 The Author(s). Published by Elsevier Ltd. This is an open access article under the CC BY-NC-ND license (<http://creativecommons.org/licenses/by-nc-nd/4.0/>).



Fig. 1. Period photograph concerning a view of the interior of the central nave portion looking at the vault structure of the cathedral before the restoration and the consolidation works (1926–28).

Heyman's principles (Heyman, 1966) to represent stress in masonry vaults. This method models the stresses as a network of forces, achieving equilibrium with gravitational loads. A contribution to the development of the method was given by O'Dwyer (O'Dwyer, 1999), while Block and colleagues substantially advanced its development in recent years (Block and Lachauer, 2014; Block, 2009). Additional methods for simulating stresses in masonry vaults are discussed in (Fraternali, 2010; Angelillo et al., 2010; Tralli et al., 2014). In 2017, a reformulation of the TNA proposed by Block was presented (Marmo and Rosati, 2017). This updated version of the TNA eliminates the need for graphical interpretation and bypasses the use of the dual grid. Their focus is only on the primal grid. This led to a substantial enhancement in the computational performance.

The updated version of the Thrust Network Analysis (TNA) allows to consider in the analysis the contribution of the horizontal forces and introduces features like free edges or holes in the vaults. This approach has been implemented in various case studies, encompassing helical staircases (Marmo et al., 2018a) and fictile vaults (Marmo et al., 2018b). In the present work, we employ the TNA reformulation presented in (Marmo and Rosati, 2017) to evaluate limit configurations of the thrust network, generally denoted as the deepest and shallowest solutions. Furthermore, the TNA is used to emulate the vault minimum thickness, to determine the vault geometric safety factor. Also, the effect of horizontal forces is studied, showing the weaknesses of the considered structure. Finally, results obtained by the TNA of the vault subjected to ordinary loads (vertical) are correlated with the AE localization to interpret the actual structural behaviour.

## 2. The monitored structure and the weak point of the central nave

In recent years, the assessment of damage progression in a specific section of the structure situated in the lower levels of the tall masonry building, particularly the bell tower, has been conducted. This evaluation involves the cumulative count of acoustic emissions (AEs) and various parameters capable of forecasting the temporal progression of damage development, as detailed in (Manuello et al., 2020). The location of Turin's Cathedral was once the site of the old Roman city's theater (13 BCE). Three separate churches—one each honouring the Holy Saviour, the Virgin Mary, and St. John the Baptist—were part of the first Christian sacred house. Some traditions state that Agilulf, the King of northern Italy from 591 to 613, continued the latter's consecration. Between 1490 and 1492, the three churches were completely destroyed. Under the direction of Amedeo de Francisco di Settignano, also referred to as Meo del Caprina, construction on the new cathedral, which would once again be named for St. John the Baptist, started in 1491. Seven years were needed to complete the church. But the bell tower stayed the same, built in 1469 and is visible today. The original design underwent various revisions in the seventeenth century thanks to Filippo Juvarra. In 1515, Pope Leo X formally proclaimed it to be the metropolitan church. When Bernardino Quadri arrived in Turin from Rome to Charles Emmanuel II of Savoy's court in 1649, plans were initiated to expand the cathedral and provide a more opulent place for the Shroud. With an oval chapel behind the choir, Quadri's design was based on a prior Carlo di Castellamonte concept. Guarino Guarini was invited in 1667 to finish the project. 1694 saw the completion of the naves and the dome. Before the work of Guarino Guarini in 1656 there was a partial collapse of the vault of the central nave, news of which was exclusively obtained from subsequent investigations performed on the vault itself. The collapsed portions were repaired with local and very circumscribed interventions. This last evidence leads to the exclusion of the hypothesis of complete reconstruction. Iron chains were inserted, one on the top, tangentially to the extrados, and one lower above the shutters. At the end of the sixteenth century, to host the Holy Shroud, Carlo Filiberto of Savoy decided to build a chapel, between the Cathedral and the Royal Palace. In this regard, the historical analysis of the Cathedral emphasized that the current structure is a culmination of various events and interventions, resulting in a heterogeneous condition concerning both materials and the employed consolidation techniques. On the foundations of the three early Christian churches, Renaissance architecture was mainly realized in marble and masonry structures. The first need for a structural intervention arose in 1656 following a partial collapse of the vault in the central nave. The implementation of the iron chains, positioned on the lower surface of the shutters and the tangential side, facilitated the consolidation of the vault until the subsequent interventions of the twentieth century. These interventions had a substantial impact on the structure of the church attic, ultimately shaping its current configuration. In particular, in 1928 the vault was found structurally unstable with excessive deformations and irregular profiles, opening phenomena localized at the extrados to the kidneys and at the intrados in the vault key. At the same time, the pillars were characterized by eccentric loading conditions as a result of an excessive filling on the sides, resulting in overhanging phenomena at the center of the nave. Intending to eliminate the unsightly chains, the Technical Commission for the restoration of the Cathedral in the period 1926–1928 pursued the aim of reducing the weight of the vault in key and to contain the thrust and the opening at the vault realized a quite invasive intervention. The barrel lowered vault with lunettes was hooked by iron tie-rods, and connected steel beams posed orthogonal respect to the axis of the vault. In particular, along the entire vault extension, there are 13 pairs of beams with double T sections that, passing through large blocks of reinforced concrete, 13 on each side, are anchored to concrete tie-beams above pillars and side walls (see, e.g., Figs. 4 and 5). For each pair of beams, 4 tie-rods that punctually sustain the structure, were



Fig. 2. Period picture, showing the same shot as in the previous picture, representing the condition of the cathedral after the works (1926–1928). The first, glaring evidence is the removal of chains at the arches of the vault in the nave.

hooked at the lower side of the vault. This solution is questionable for several reasons: although the combined system of concrete blocks, steel beams, and concrete tie-beams forms a framework that aids the side walls in absorbing horizontal thrusts transmitted from the vault, placing large masses at the top of structures is highly disadvantageous from the seismic point of view. In addition, even under static loads, the effect of tie-rods generates concentrated force directed upwards which compromises the transmission of compression forces through the vault reducing its stiffness and stability.

In the following two period photographs are reported, the first concerns a view of the interior of the central nave before the restoration and the consolidation works that took place (1926–28) see Fig. 1. These works represent the last main intervention on the structural part of the cathedral, except for the consolidation of the Holy Shroud dome after the 1997 fire. The second period picture, showing the same shot, represents the condition of the cathedral after the restoration works. The first, glaring evidence, is the removal of chains at the arches of the vault in the central nave see Fig. 2. In order to better clarify the building techniques historically employed, the materials and the configuration of the different reinforcements adopted over time, the schemes in Fig. 3 are reported. Above, a schematic transversal section of the roof level is shown with the evidence of the reinforcing steel beams and the layout of the concrete blocks, put in place during the extensive retrofitting work. The original vault, partially rebuilt in 1656 has a thickness of 280 mm and is realized by brick masonry, the steel reinforcing paired beams are 220 mm high with a variable span between 12.0 and 12.5 m. The concrete elements (blocks) with a dimension of about  $1.0 \times 1.60 \times 1.60$  m are 13 blocks for each side and house the steel beams that are embedded

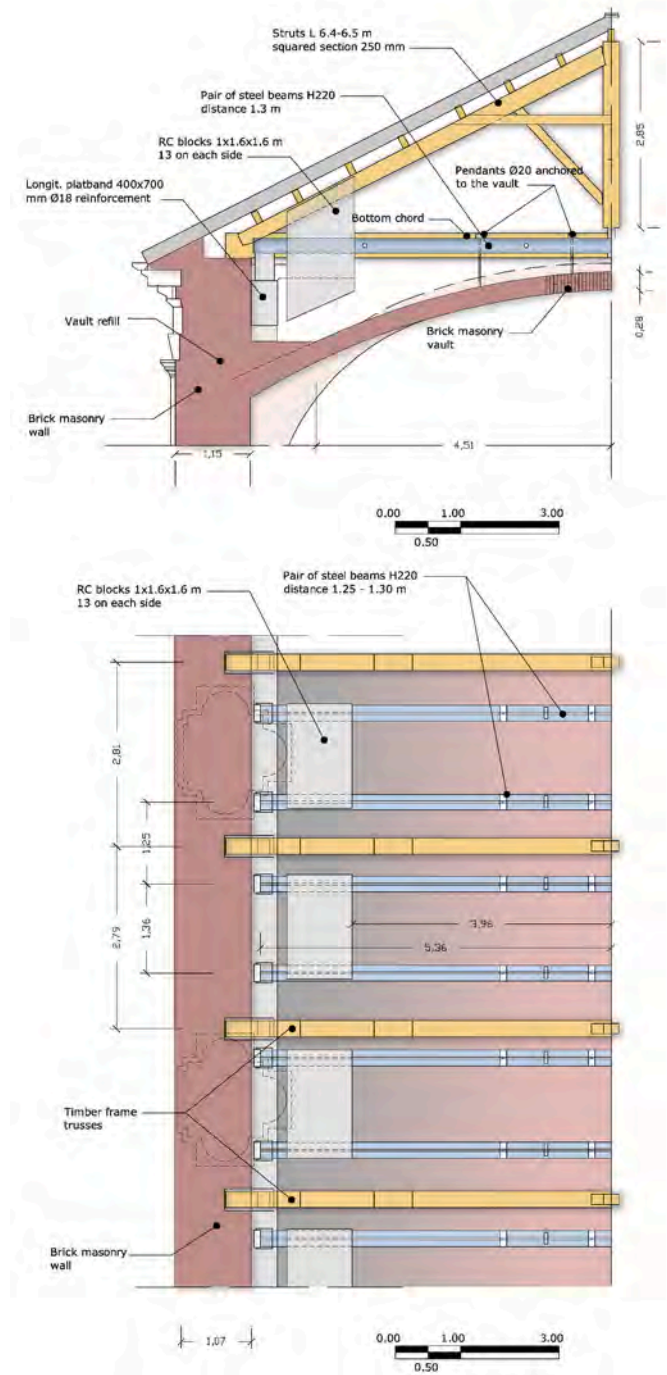


Fig. 3. Positioning of the original timber trusses and of the reinforcing paired steel beams posed in 1926–28. The works involved the removal of chains inside the church the placement of pendants and blocks.

within them near the connection to the historic masonry brick walls on the longitudinal sides above the nave. The steel beams rest on a reinforced plat band of  $400 \times 700$  mm in size running on both sides and are connected to each other spacers (circular section  $\varnothing 32$  mm). The steel beams, paired two by two, are connected to the vault with pendants (circular section  $\varnothing 20$  mm) that were placed to support the roof after the removal of the original 17th-century chains see Fig. 2. These plat bands are connected with the perimeter walls (sustained by the composite pillars) by punctual supports realized with masonry old bricks. In the joined picture the partial representation of the plan at the underfloor level is also reported. In this picture, the positioning of the timber frame



Fig. 4. Overall photo of the wooden trusses in the attic of the central nave.



Fig. 5. Concrete blocks and coupled iron supporting beams.

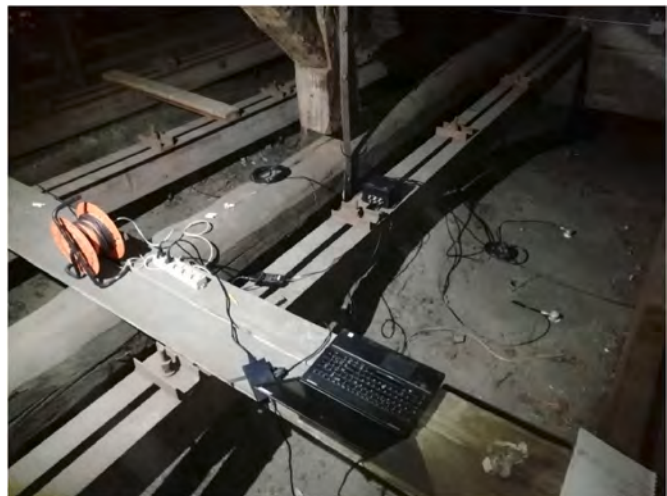


Fig. 6. AEmission System: Multi-channel acquisition system and sensors applied to the vault extrados.

trusses and of the steel beams together with the concrete blocks are shown with the spacing dimension 2.80 m for the timber structures and 1.30 for the paired steel beams Fig. 3. The monument holds a heritage value of the highest level and the importance of its conservation appears to be a matter of strong interest due to the fact that the structures of the cathedral nave are connected to the chapel containing the Holy Shroud of Turin. The monument is thus made up of intersecting and connected elements of absolute historical and architectural value. The stability of



Fig. 7. Two of the eight sensors, positioned on the extrados of the central nave vault.

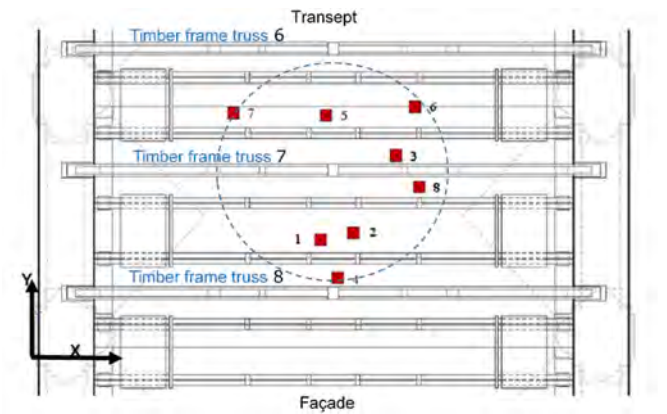


Fig. 8. Locations of the pzt transducers between timber frame trusses 6 and 8. The positions are reported in meters respect to the reference system shown in the picture (see Table 1).

Table 1

Sensor position [m].

Sensors	S1	S2	S3	S4	S5	S6	S7	S8
x coordinate	6.35	7.07	8.02	6.74	6.47	8.44	4.42	8.54
y coordinate	2.60	2.75	4.45	1.76	5.33	5.52	5.38	3.76

the nave that is the subject of the present work is of fundamental importance for the integrity of the structure that, through the transept and the presbytery, are connected to the lantern of the dome Holy erected in 1694 b y the architect Guarino Guarini.

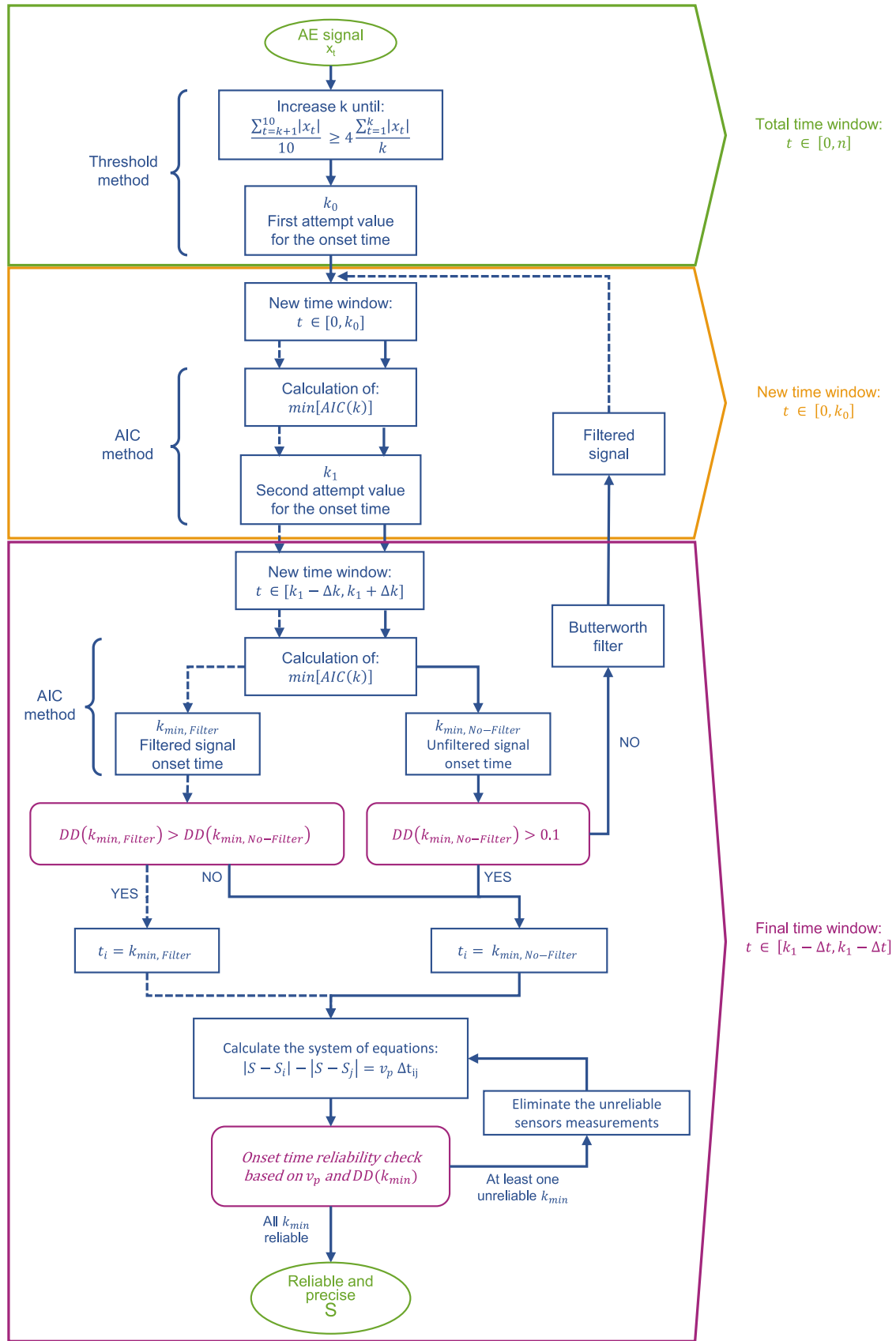


Fig. 9. Improved AIC method workflow.

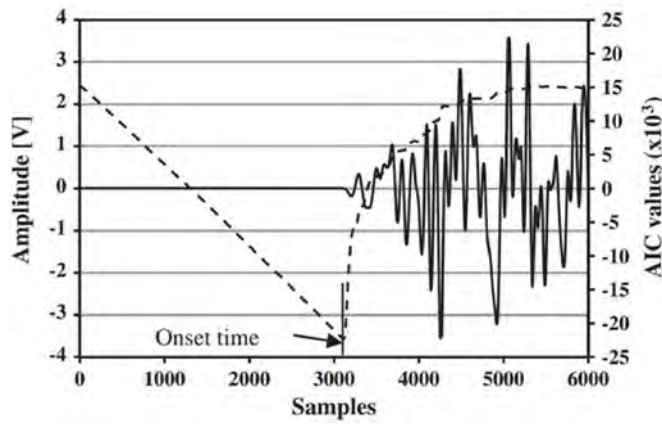


Fig. 10. Only the chosen portion of the signal that contains the onset, shown by the solid line, is utilized to determine the onset time using the AIC value. The signal's onset time is shown by the dashed line, which represents the minimum value of the AIC function.

### 3. AE monitoring analysis and methods

A set of 8 piezoelectric (PZT) transducers is connected to an acquisition system which supports up to 10 input channels. Monitoring time extended for four months from September 2020 to January 2021. There

is a 64 MB dedicated RAM for each channel. This system captures, processes, and analyzes the essential properties of the detected Acoustic Emission (AE) signal waveforms automatically and in real-time. The signal start time, average frequency ring down counts, peak amplitude, cumulative event count, and signal duration are some of these metrics. Based on the collected data, on-field damage localization and quantification are made easier by automatic processing. The GPRS/UMTS system transmits the processed data to a remote server, allowing for the simultaneous and continuous monitoring of specific structural parts. Each channel is composed of an ADC (analog-to-digital converter) module with a sampling rate of 10 mega-samples per second. This rate covers the normal frequency range of broadband PZT sensors typically used in structural monitoring applications and is sufficient to capture frequency components up to 1 MHz. When it comes to Acoustic Emission (AE) monitoring, the average frequency range of signals originating from sources and micro-cracks in materials such as concrete and masonry is between 50 kHz and 350 kHz (Carpinteri et al., 2013b). Notably, the AE device's 10 mega-samples per second (Ms/s) sampling rate is 200–50 times higher than the frequency of the AE signals linked to the advancement of damage. The study's Acoustic Emission (AE) apparatus allowed for the freedom to choose the best threshold value based on the unique features of the structure under observation and the surrounding environmental circumstances. The apparatus used two different modes to calculate threshold values in terms of amplitudes. These values function as the benchmarks, above which the signal is appropriately recognized and documented. Generally speaking, the signal threshold

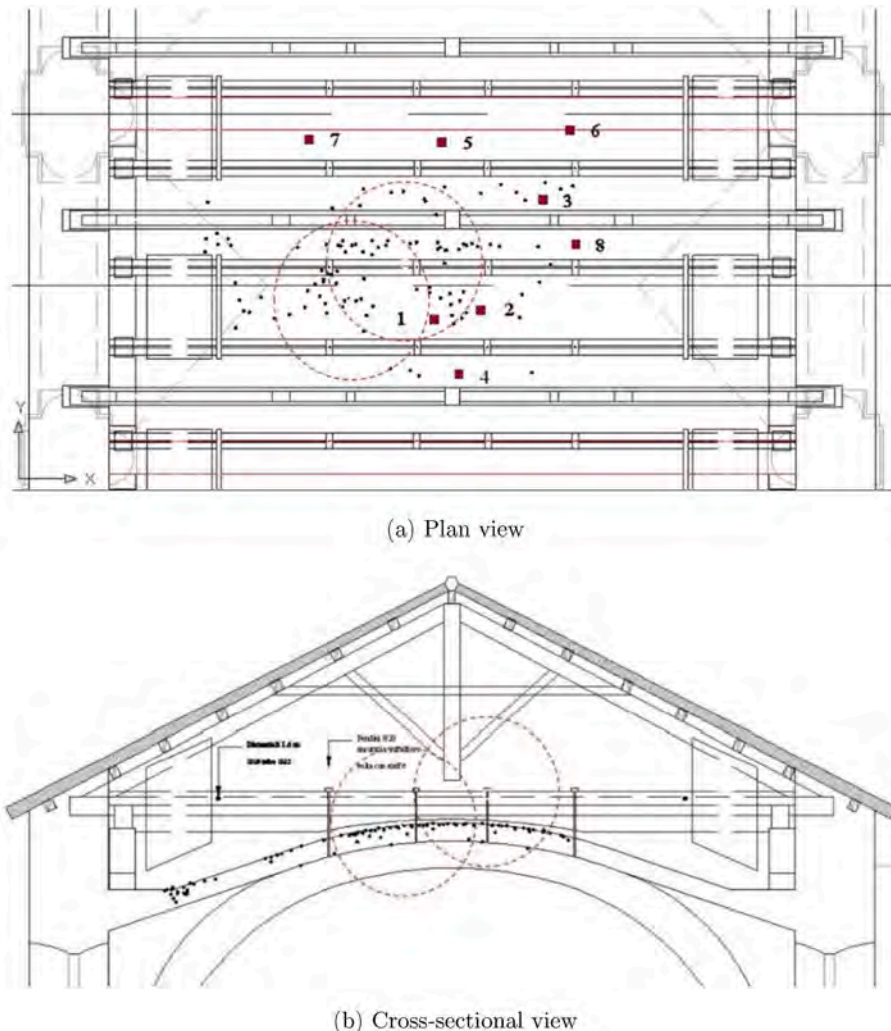


Fig. 11. Localization of Acoustic Emission sources.

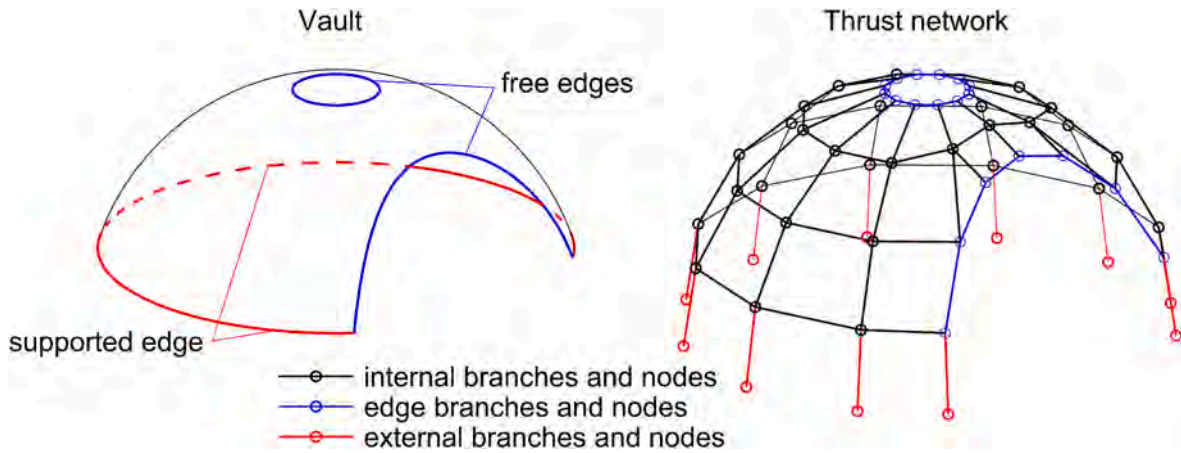


Fig. 12. A vault and the corresponding thrust network, with the classification of branches and nodes.

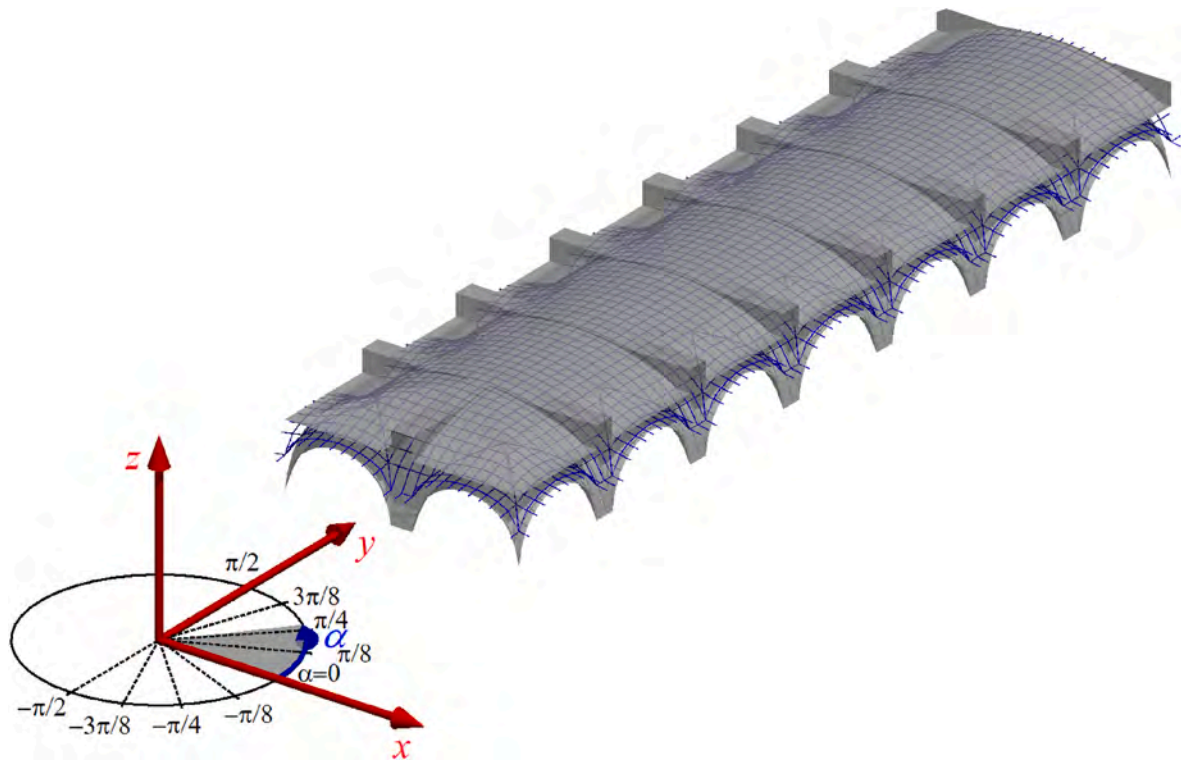


Fig. 13. The thrust network's initial configuration used for analyzing the equilibrium of the central nave vault.

value is set between 50  $\mu\text{V}$  and 100 mV. These values were recognized and set according to several laboratory and in situ experiments, performed by the same AE device, on concrete, reinforced concrete, rocks, brick-based and stone masonry (Anzani et al., 2008; Lacidogna et al., 2015; Niccolini et al., 2011b). Finding the ideal threshold for each sensor combination is made possible by the AE device's extensive threshold setting flexibility. This is dependent upon the particular operational circumstances in which the observation is being conducted, as emphasized by Carpinteri et al. in their work on reliable monitoring (Carpinteri et al., 2012). There are several potential origins and external circumstances of background noise, including mechanical, electromagnetic, human-induced, and environmental influences. In most cases, the tendency is to choose a low threshold level in order to avoid unintentionally excluding significant data. This method seeks to achieve a compromise between reducing the possibility of missing important information because of high threshold settings and maintaining the threshold's sensitivity to detect relevant signals.

The threshold methods used in various approaches were integrated into the device's software, as the authors have revealed and documented in several papers (Lacidogna et al., 2015; Carpinteri et al., 2012).

The AE apparatus performs several analyses automatically. The first parameter, which is the total number of AE events found throughout the monitoring period and is represented as the cumulative number of AE signals  $N$ . Moreover, the rate of propagation of micro-cracks in the time domain may be linked to the temporal development of structural damage seen throughout the monitoring period, represented by the parameter  $\beta^t$ .

In Figs. 6 and 7 the AE equipment application is reported. In particular, the multi-channel acquisition system and PZT sensors applied to the vault extrados are reported. When the vaults were being monitored, the localization of Acoustic Emission (AE) sources was conducted to pinpoint the corresponding cracks in a 3D model. In the initial localization step, all signals recorded by various sensors that fall within a time interval compatible with the development of micro-cracks are

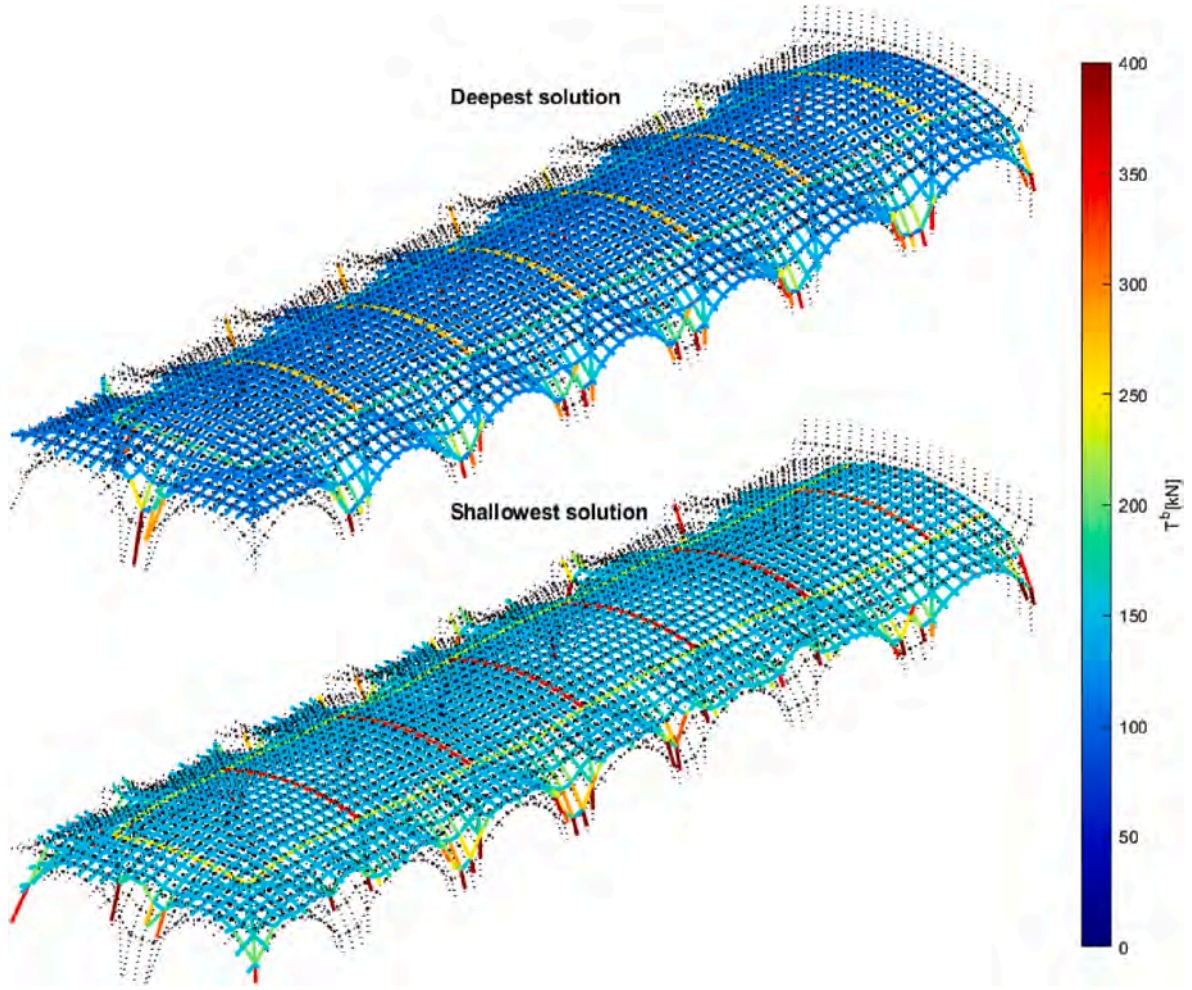


Fig. 14. Deepest and shallowest solutions for the vault subjected to vertical loads only ( $r_s/r_d = 0.78$ ).

identified and grouped. The signals recognized belonging to the same crack advancement and propagation, are characterized by a time delay of the order of microseconds. In the early studies focused on Acoustic Emission (AE) localization in concrete structures (Li and Shah, 1994), it was common an assumption of 100 mV as a threshold on the amplitude of the elastic wave in order to identify the onset time of the P-wave. The traditional formulation of the AE localization problem can be expressed as:

$$d_i - d_j = v_p \Delta t_{ij} \quad (1)$$

In the equation,  $v_p$  represents the velocity of the elastic waves. The velocity can be estimated as a variable correlated to the level of damage. An alternative simplified approach is to assume the velocity as a material constant. At the same time,  $\Delta t_{ij}$  is the difference in the arrival time of the signals to sensors  $i$  and  $j$ .

The AE source localization can be performed in two ways: considering at least 5 sensors and consequently a 4-equation system where the elastic wave velocity ( $v_p$ ) is unknown, or alternatively, at least 4 sensors and a 3-equation system, where the unique unknown are the 3D coordinates of the source and the velocity is considered known a priori. The first case, that is the case used by the authors in the present paper, the velocity of the elastic P-wave is obtained as an unknown, this fact allows to use the velocity as a further estimation parameter of the mechanical properties of the material changing during the monitoring time and secondly, the extraction  $v_p$  in the 4-equation system lead to a more precise estimation of the localized AE sources. The variables involved in the AE localization process are the coordinates of the AE source ( $x, y, z$ )

and the elastic wave propagation speed. To localize each micro-crack, various groups, each consisting of at least 5 sensors, need to be identified. The velocity  $v_p$  can be calculated as:

$$v_p = \sqrt{E(1-\nu)/(\rho(1+\nu)(1-\nu))} \quad (2)$$

and in the case concrete or masonry structures it can be assumed  $\nu = 0.2$ :

$$E = 0.9(v_p^2 \rho) \quad (3)$$

Regarding the propagation speed of elastic waves in the medium it was not assumed a priori by the authors but is rather considered as a variable in the system of equations that allows the location of the crack sources. In fact, by composing a system of at least four equations of the type of Eq. (1) it will be possible to obtain as output results the three coordinates of the source and the propagation velocity of the signals associated with that source propagation (P-wave). In this case in order to be able to write at least 4 equations of the type of Eq. (1) a set of at least 5 sensors must have acquired the signals corresponding to the same microcrack. From this point of view, the localization procedure is based on Eq. (1) and is referred to well-known procedures reported in several publications also by the same authors (Anzani et al., 2008; Li and Shah, 1994; Lacidogna et al., 2015; Niccolini et al., 2011b; Carpinteri et al., 2012). The wave propagation velocity obtained by the localization procedure based on the triangulation method ranges between  $1.08 \times 10^3$  and  $1.85 \times 10^3 \text{ ms}^{-1}$ . The frequency range is between 120 and 190 kHz and consequently, the mean wavelength is about 0.015 m. Regarding attenuation, an accurate estimation would require ad hoc

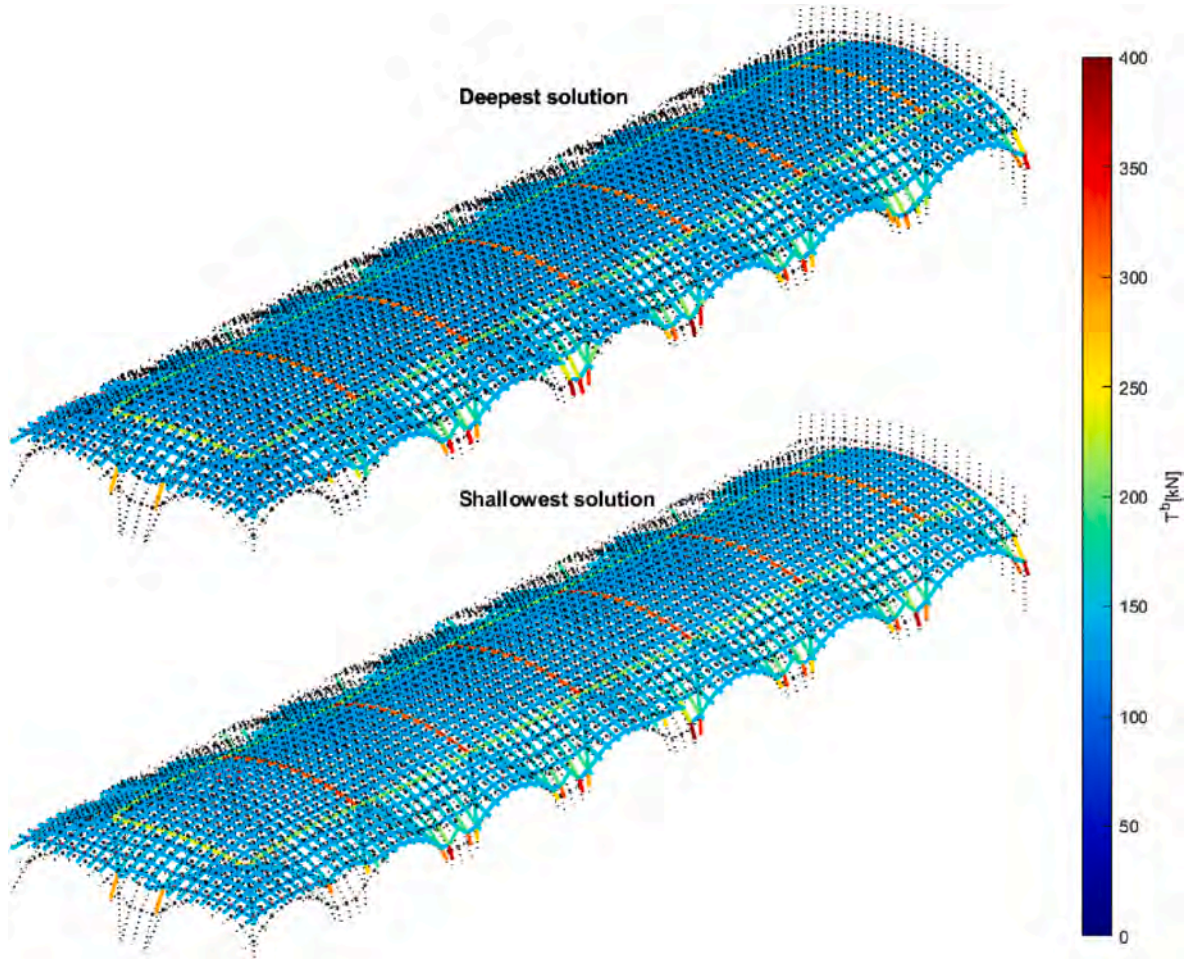


Fig. 15. Deepest and shallowest solutions for the vault subjected to vertical loads only and characterized by the minimum thickness ( $T_{\min}/T = 0.63$ ,  $r_s/r_d = 1$ ).

tests in order to estimate the attenuation parameter according to the common frequency-dependent pattern in attenuation described by the power-law. In this case, the authors considering similar cases and measurements performed in the laboratory on brick masonry (Q et al., 2015) concentrated the sensor placements within a radius of 2.8 m from the barycenter of the sensor set (see Fig. 8).

The elastic modulus of the material  $E$  can thus be correlated to the evolution of the damage (Lenticchia et al., 2021). The accuracy of AE localization can be influenced by various factors, including the signal-to-noise ratio, electronic noise in the instrumentation, and the onset time picking procedure. Regarding the latter, several methods were adopted to identify the optimal onset time at each sensor (Melchiorre et al., 2023b). Based on this, the improved Akaike Information Criterion (i-AIC) picker method can be utilized. The i-AIC method, grounded in the Akaike information criterion, is directly integrated into the Acoustic Emission (AE) code employed for source localization, as illustrated in Fig. 9.

According to this method, the signal is considered as an auto-regressive model:

$$x_t = \sum_{k=1}^N a_m^i x_{t-m} + e_t^i \quad (4)$$

The signal is divided into two intervals. The first time interval is the one with  $t = 1, \dots, k$  while the second one is characterized by  $t = k + 1, \dots, n$ . The original AIC criterion may be used to identify the point between two neighbouring time series. This implies that it can be employed to differentiate the actual signal from the background noise, given their distinct underlying statistics. The method was initially

developed to estimate the best order of the auto-regressive process fitting the time series in seismology (Sleeman and Van Eck, 1999; Earle and Shearer, 1994; Tong and Kennet, 1996; Withers et al., 1998; Anant and Dowla, 1997). The model incorporates a time series comprising both a deterministic and a non-deterministic component. The non-deterministic time series  $e_t^n$  or noise is assumed to follow a Gaussian distribution. The Maximum Likelihood Estimation (MLE) method, based on the Akaike Information Criterion (AIC), is employed to separate the time series into intervals  $[1, k]$  and  $[k + 1, n]$  using Eq. (4). The approximate likelihood function  $L$  can be expressed as the joint Probability Density Function for the two non-deterministic time series.

$$L(x; k, M, \Theta) = \prod_{i=1}^2 \frac{1}{\sigma_i^2 2\pi} \exp \left[ -\frac{1}{\sigma_i^2} \sum_{k=1}^N (a_m^i x_{j-m} + e_t^i)^2 \right] \quad (5)$$

where  $\Theta_i(\Theta(a_1^i, \dots, a_M^i))$  represents the model parameters ( $\sigma_i^2$  is dependent on  $k$ ), and  $p_1 = 1, p_2 = k + 1, n_1 = k, n_2 = n - k$ . As commonly understood, The Maximum Likelihood Estimation (MLE) technique finds the precise model parameter values that maximize the likelihood function  $L$ , or make the observed outcomes the most likely. In operational terms, it will act considering the AIC Criterion formulation can be reformulated by considering the two segments of the signal: one containing the actual signal and the second one characterized by white noise. This yields:

$$AIC(k) = k \log(\sigma_{1,\max}^2) + (n - k) \log(\sigma_{2,\max}^2) + 2C \quad (6)$$

where the two  $\sigma_{1,2,\max}^2$  represent the variances of the two times series considering the stationary condition of the maximization procedure and

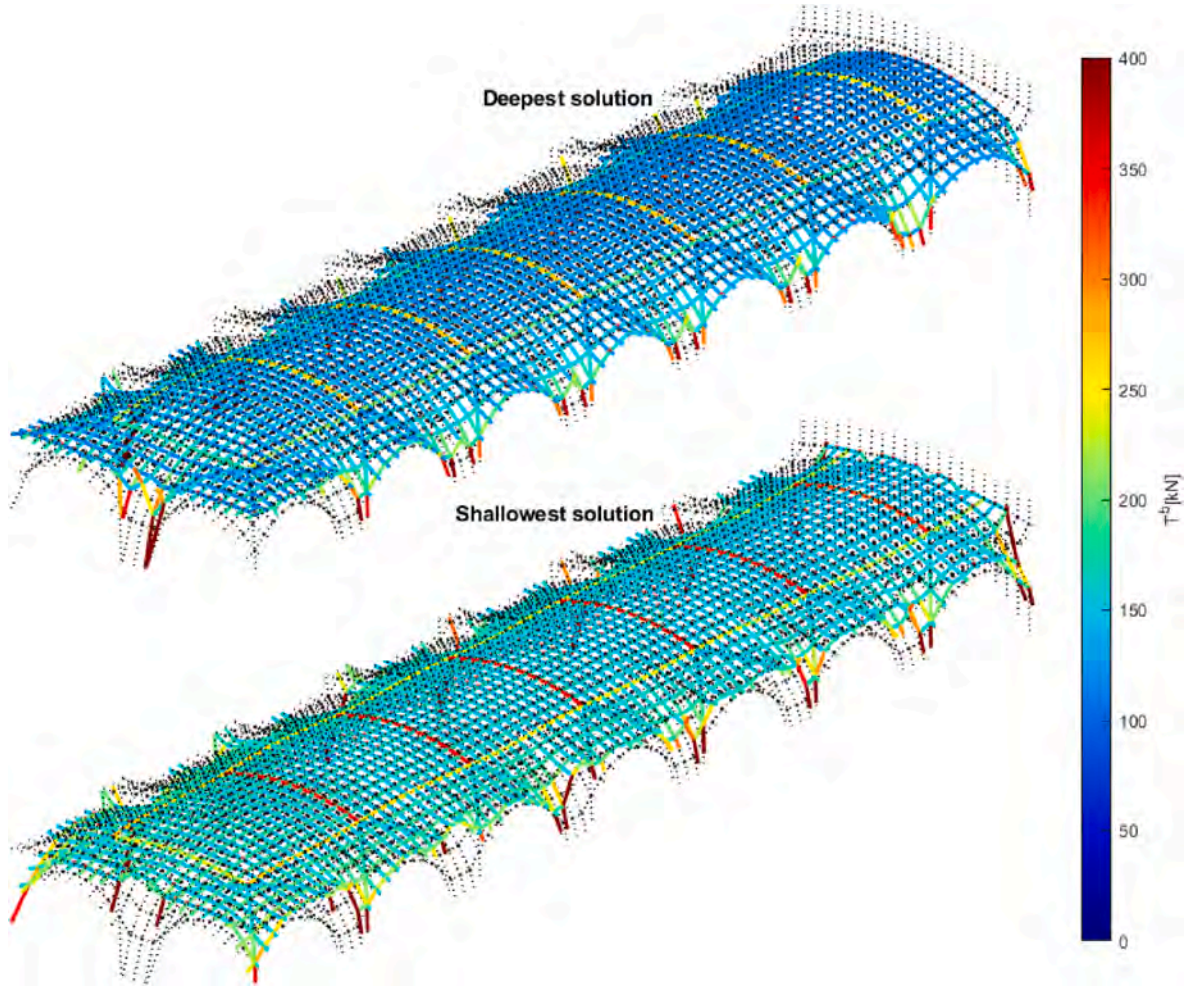


Fig. 16. Deepest and shallowest solutions for the vault subject to vertical and horizontal loads ( $\lambda = 0.057$ ,  $\alpha = -\pi/2$ ).

$C = \frac{-n}{2}(1 + \ln 2\pi)$  is a constant value. In the given relationship, The uncertainty is represented by the second term, whereas the disparity in the model's fit is represented by the first. The ideal split of the two time series is defined as the point  $k$  at which the joint likelihood is maximized or  $AIC(k)$  in (6) is reduced. This moment is considered to be the phase start since it yields the best match for both models. If the goal is to identify the P-wave's onset alone, choosing a suitable time window that includes the onset time is also essential. This method is known as AIC-picker in practice, and the  $AIC(k)$  value is defined as:

$$AIC(k_w) = k_w \log(\text{var}(R_w(1, k_w))) + (n_w - k_w) \log(\text{var}(R_w(1 + k_w, n_w))), \quad (7)$$

where  $w$  indicates that only the selected interval containing the onset time is taken rather than the whole time series. The last sample in the current time series,  $n_w$ , has a range of 1 to  $n_w$  for  $k_w$ . The variance computed from 1 to  $k_w$  is denoted by the phrase  $\text{var}(R_w(1, k_w))$ , but all samples ranging from  $1 + k_w$  to  $n_w$  are taken into consideration when  $\text{var}(R_w(1 + k_w, n_w))$  is used. The initial P-wave onset time of the AE signal is defined by the global minimum of the AIC function (see Fig. 10).

As previously noted, AIC-picker yields superior results when AIC is specifically applied to a pre-defined window within the time series that encompasses the onset time. In the automatic algorithm, the P-time is initially determined using a straightforward method based on a threshold amplitude, as outlined in (Carpinteri et al., 2012):

$$\sum_{i=k+1}^{10} |x_i|/10 \geq 4 \sum_{i=1}^k |x_i|/k \quad (8)$$

Using this equation, the moving average amplitude of a set composed

of 10 data points is compared to four multiplied by the mean amplitude of the time series interval spanning from 1 to  $k$ . The initial value of  $k$  that fulfils Eq. (8) is designated as the first trial onset time ( $k_0$ ). The initial estimation consistently falls after the actual onset time. Taking this into account in the AIC application, two types of time windows with distinct intervals are successively defined. Initially, the algorithm is applied to the interval  $[1, k_0]$  (window 1), serving for a preliminary determination of the onset time through AIC, resulting in the value  $k_1$ . The second time window (2) is centred around the value  $k_1$  with a length of  $2\Delta k$ . The value of  $\Delta k$  is contingent on the sample frequency. In our investigation, with a sampling frequency of 10 MHz, choosing  $\Delta k$  equal to 3000 samples yields optimal results. The onset time, corresponding to the  $k_{min}$  value obtained from the AIC-picker within the time window (2), is considered as the actual onset time of the analyzed AE signal. Fig. 11a) and 11b) depict the results of the AE localization utilizing the enhanced AIC-picker method, as detailed in (Carpinteri et al., 2012).

#### 4. Equilibrium analysis of the central nave vault

As observed by Heyman in 1966 (Heyman, 1966), the stresses that lead to failure in masonry vaults are typically lower than those required for material failure. Consequently, the stability of such structures is primarily dictated by their shape and the distribution of self-weight (Huerta, 2006).

According to Heyman's safe theorem of the limit analysis of masonry arches, if a thrust line wholly contained within the arch thickness and in equilibrium with external loads exists, then the structure is safe. Its

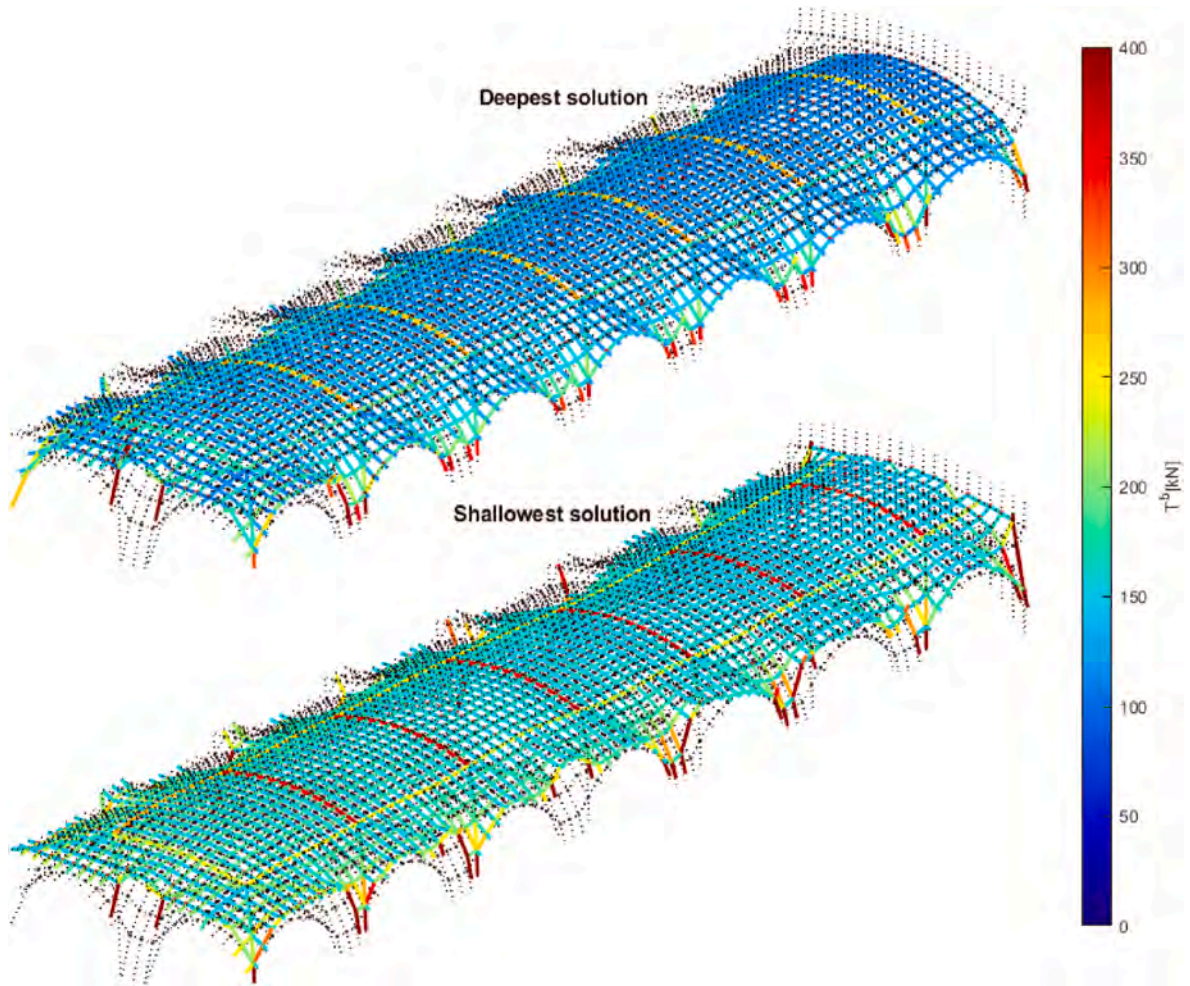


Fig. 17. Deepest and shallowest solutions for the vault subject to vertical and horizontal loads ( $\lambda = 0.074$ ,  $\alpha = -3\pi/8$ ).

extension to the limit analysis of masonry vaults can be done by verifying the existence of a thrust surface wholly contained within the vault thickness and in equilibrium with external loads. Such an extension promptly allowed for the development of analytical solutions proposed by the same Heyman for the analysis of domes (Heyman, 1967) while several numerical solutions have been proposed for the analysis of generic vaults, see, e.g., (Angelillo and Fortunato, 2004; Fraddosio et al., 2020).

The determination of thrust surfaces in masonry vaults depends on the geometry of vault intrados and extrados, and on the distribution of loads, while vault stereotomy is usually neglected. Such simplifying assumption usually leads to conservative results and significant effects imputable to stereotomy are noticed only for uncommon block arrangements (Gáspár et al., 2018).

A discretized representation of the thrust surface can be obtained by representing membrane stresses within the surface as a discrete network of forces. This assumption led to the development of the Thrust Network Analysis (TNA) (O'Dwyer, 1999), although the current nomenclature is due to Block and Ochsendorf (2007). The TNA substitutes the geometry of the thrust surface by a finite number of network nodes whose position is subjected to geometric constraints represented by the vault intrados and extrados, while network branches, connecting pairs of nodes, represent the line of action of the internal forces. Accordingly, the analysis is conducted by finding a network whose nodes are wholly contained within the vault thickness and whose axial forces in branches are compressive. While the existence of at least one solution is sufficient for the assessment of structural safety, the problem may either admit no

solutions, when the structure is unsafe, one unique solution, which represents a limit condition for the structural equilibrium, e.g. when the thickness reaches its theoretical minimum, or infinitely many distinct solutions. In this last case, the set of all possible solutions is bounded by the so-called solutions of minimum and maximum thrust, corresponding, in general, to a deeper and shallower configuration of the thrust network. As these two boundaries tend to coincide, the structural equilibrium is closer to a limit condition. Accordingly, one can infer the distance from the limit condition, or the safety factor, from the distance between these two boundary solutions.

For the thrust network analysis of the vault of the Turin Cathedral central nave we employ a recent implementation proposed in (Marmo and Rosati, 2017), which also includes the effects of free edges and horizontal loads. Before reporting the result of such an application, we include hereafter a summary of the method for the reader's convenience.

#### 4.1. Thrust network analysis

The equilibrium of a masonry vault can be assessed by modelling the internal forces through a network of thrusts in equilibrium with the applied loads. This *thrust network* is characterized by  $N_n$  nodes and  $N_b$  branches. The thrust network functions as a representation of the thrust forces responsible for maintaining equilibrium with external loads. Consequently, the branches of the network indicate the line of action of thrust forces, akin to the sides of a funicular polygon.

In a three-dimensional Cartesian reference frame with a vertical direction  $z$ , the  $n$ -th node of the network has position  $\mathbf{p}_n = (x_n, y_n, z_n)$ .

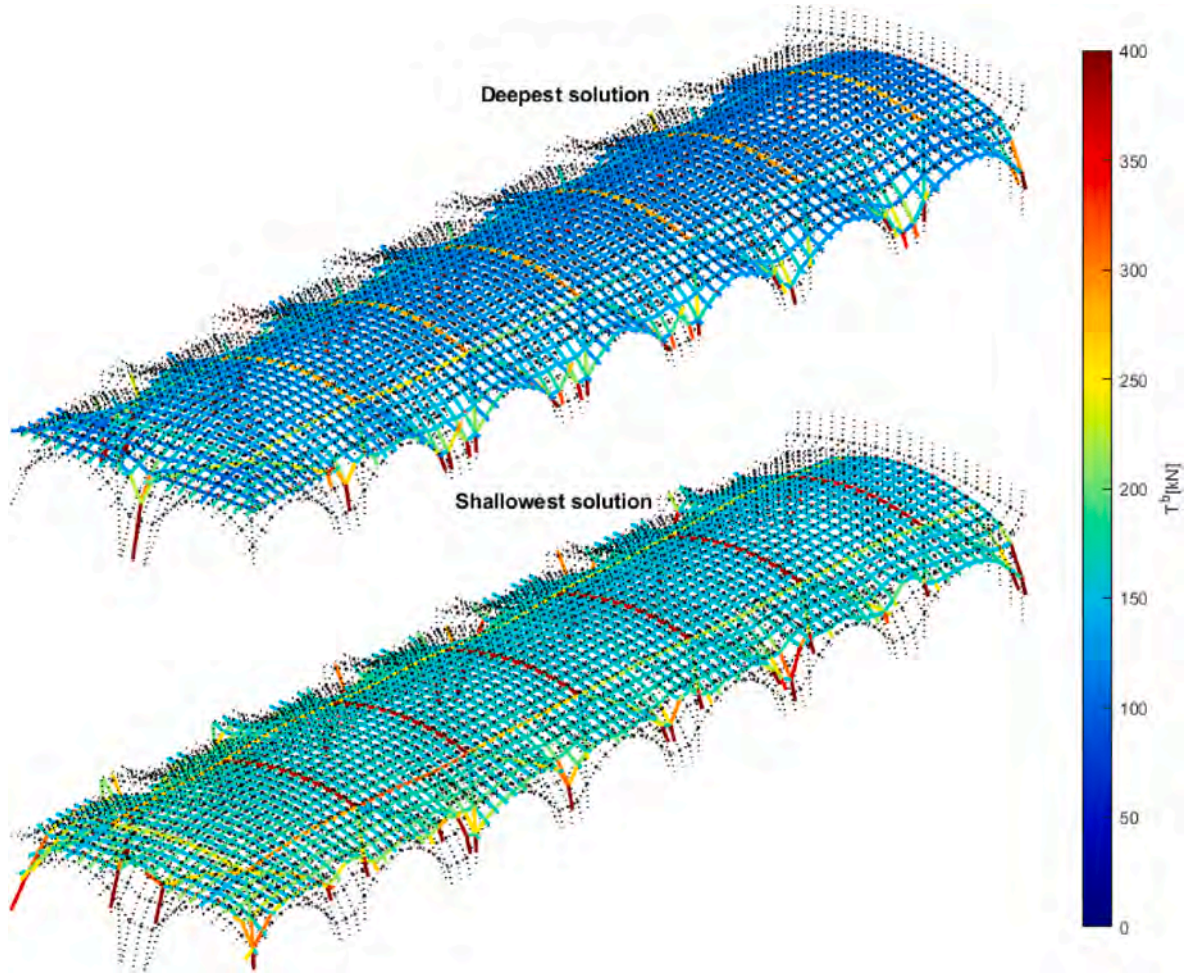


Fig. 18. Deepest and shallowest solutions for the vault subject to vertical and horizontal loads ( $\lambda = 0.094$ ,  $\alpha = -\pi/4$ ).

Nodes are subjected to an external force  $\mathbf{f}^{(n)} = (f_x^{(n)}, f_y^{(n)}, f_z^{(n)})$ , and the magnitude of this force is contingent on the node's region of influence.

Each branch  $b$  of the network connects two nodes of the network and represents the thrust force  $t^{(b)}$  transmitted between such two nodes. Due to the compressive nature of the thrust forces, they are directed toward the generic node  $n$ , so that they can be represented as a vector  $\mathbf{t}^{(b)} = (t_x^{(b)}, t_y^{(b)}, t_z^{(b)})$  laying on the branch.

Branches can be classified as *internal*, representing thrust forces that are contained within the network, *edge*, representing forces located on free edges, or *external*, representing the support reactions, as shown in Fig. 12. Similarly, the group of nodes can be categorized into  $N_i$  internal nodes,  $N_e$  edge nodes, and  $N_r$  restrained external nodes, with only one external branch converging. This configuration leads to a total of  $N_n = N_i + N_e + N_r$  nodes.

The height (vertical position  $z_n$ ) of all nodes is unknown and can be obtained by specifying that the network must be funicular of applied forces. Additionally, according to Heyman's limit analysis approach, nodes have to be contained within the thickness of masonry, i.e. their height shall be contained between the intrados and extrados of the vault. While the horizontal positions of internal and external nodes are determined, the horizontal coordinates of edge nodes remain unknown. This is because the associated edge branches, those connected by edge nodes, must be funicular, maintaining equilibrium both horizontally and vertically concerning the internal thrusts and applied loads on edge nodes.

Equilibrium conditions are applied to ascertain the heights of internal and external nodes, along with the comprehensive set of coordinates

for boundary (edge) nodes and the thrust forces within branches. These equations are formulated exclusively for edge and internal nodes, as external ones only serve as endpoints for external branches.

#### 4.1.1. Equilibrium equations

The equilibrium in the horizontal plane ( $x - y$  plane) of internal nodes is enforced by the following  $2N_i$  equations:

$$\begin{cases} \mathbf{C}_i \hat{\mathbf{t}}_h + \mathbf{f}_{x,i} \mathbf{r} = \mathbf{0}_i \\ \mathbf{S}_i \hat{\mathbf{t}}_h + \mathbf{f}_{y,i} \mathbf{r} = \mathbf{0}_i \end{cases} \quad (9)$$

The coefficient matrices  $\mathbf{C}_i$  and  $\mathbf{S}_i$  in Eq. (9) are composed of the cosine directors of the horizontal projections of the network branches. It is important to note that  $i$  indicates that only the equilibrium of internal nodes is under consideration. In Eq. (9) the vector  $\hat{\mathbf{t}}_h$  comprises of the reference thrusts of branches, denoted by  $\hat{t}_h^{(b)} = r t_h^{(b)} = r \sqrt{t_x^{(b)2} + t_y^{(b)2}}$ , where  $r$  is an unknown scaling parameter, common to all branches, and  $\mathbf{0}_i$  is a vector consisting of  $N_i$  zeros.

Vertical equilibrium of all internal nodes of the network is enforced by the  $N_i$  equations:

$$\mathbf{D}_i \mathbf{z} + \mathbf{f}_{z,i} \mathbf{r} = \mathbf{0}_i \quad (10)$$

The entries of  $\mathbf{D}_i$  are calculated by aggregating the thrust densities of all internal branches. More precisely, for a branch  $b$  connecting nodes  $n$  and  $m$  of the network, the coefficients  $\mathbf{D}^{(b)}$  are computed and arranged in the rows  $n$  and  $m$  of columns  $n$  and  $m$  of a coefficient matrix  $\mathbf{D}_i$ . The coefficients result from a combination of the reference thrust densities

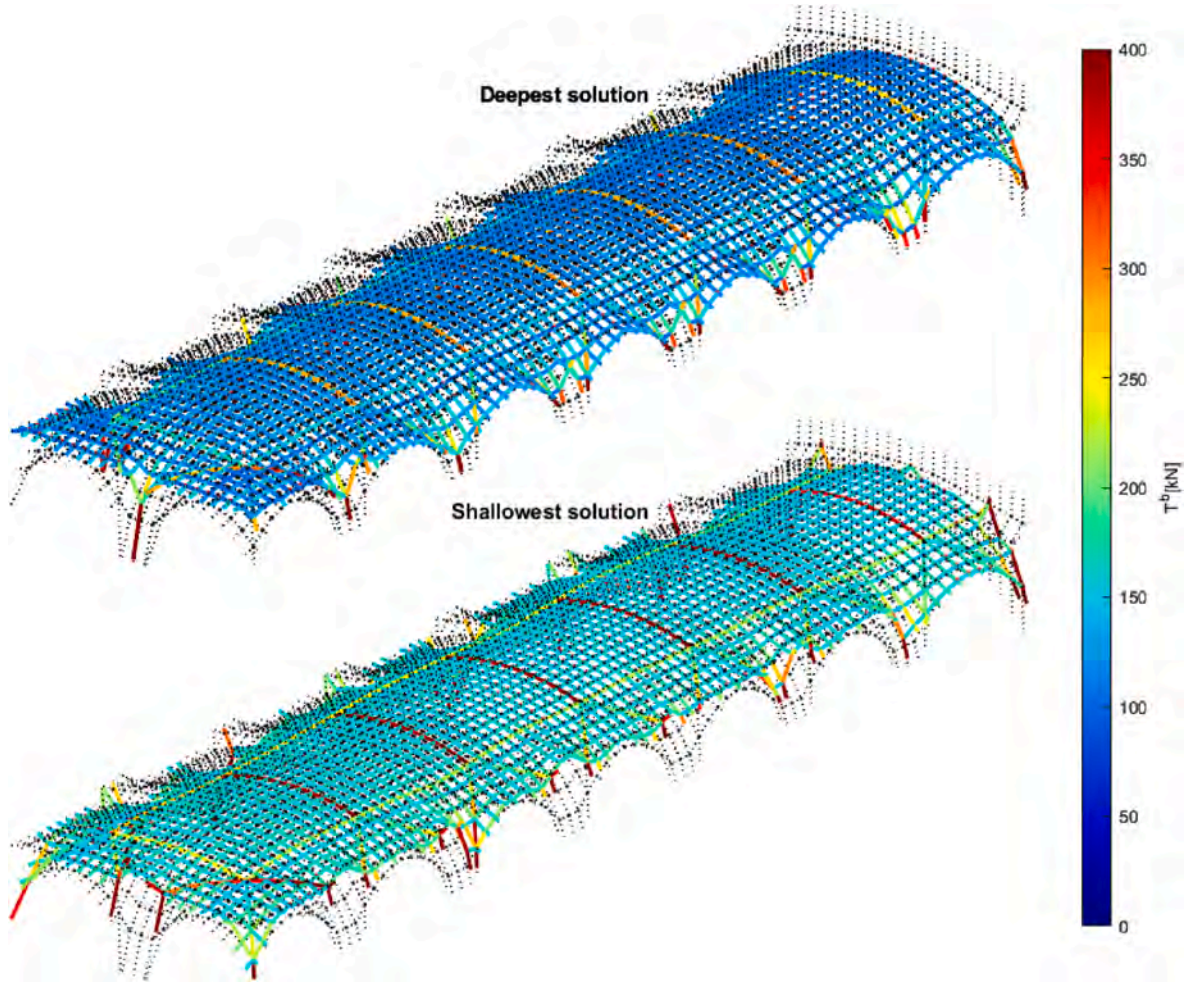


Fig. 19. Deepest and shallowest solutions for the vault subject to vertical and horizontal loads ( $\lambda = 0.105$ ,  $\alpha = -\pi/8$ ).

$\hat{\mathbf{t}}_h^{(b)} / \ell_h^{(b)}$  of the network branches, where  $\ell_h^{(b)}$  is the horizontal projection length of the branch.

The vector  $\mathbf{z}$  represents the unknown heights of all nodes, and  $\mathbf{f}_{z,i}$  is the vector of vertical loads applied specifically to internal nodes.

Eq. (10) uses the parameter  $r$  to derive multiple solutions for the same vertical equilibrium equation. This equation shows that when keeping  $\mathbf{f}_{z,i}$  constant, lower values of  $r$  result in lower values of  $\mathbf{z}$ , and higher values of  $r$  result in higher values of  $\mathbf{z}$ . Furthermore, the parameter  $r$  transforms the reference horizontal thrusts into actual horizontal thrusts using the relationship  $\hat{\mathbf{t}}_h^{(b)} = r \mathbf{t}_h^{(b)}$ . Therefore, this parameter can be utilized to obtain a balanced configuration of the network that exhibits higher thrust values, which correspond to a shallower thrust network characterized by lower values of  $\mathbf{z}$ , and vice versa. These two limit solutions are referred to as *solution of maximum thrust*, or *shallowest solution*, and *solution of minimum thrust*, or *deepest solution*, respectively. Indicating by  $r_s(r_s)$  represents the value of  $r$  associated with the shallowest configuration of the network and by  $r_d$  that associated with the deepest solution, it is always  $r_d \geq r_s$  or, equivalently,  $r_s/r_d \leq 1$ .

#### 4.1.2. Generic solving procedure

In the original versions of the TNA (O'Dwyer, 1999; Block, 2009), Eq. (9) are employed to evaluate the unknown reference thrusts. Once these are known, Eq. (10) can be used to evaluate nodal heights. Both these sets of unknowns are subjected to a series of constraints, respectively representing the no-tension assumptions for the reference thrusts and the inclusion within the masonry volume for nodal heights. Hence

these systems of equations are solved by employing constrained optimization procedures.

In the more general case considered in the recent reformulation of the method (Marmo and Rosati, 2017), Eqs. (9) and (10) are coupled by means of the unknown  $r$ , hence an iterative procedure is required to solve separately the two sets of equations. At the generic  $j$ -th iteration of such procedure it is assigned a tentative value for  $r$ , namely  $r^{(j)}$ , and the corresponding reference thrusts  $\hat{\mathbf{t}}_h^{(j)}$  are evaluated by solving the linear constrained optimization problem

$$\min_{\hat{\mathbf{t}}_h} \sum_b \hat{\mathbf{t}}_h^{(b,j)} \text{ such that } \begin{cases} \begin{bmatrix} \mathbf{C}_i \\ \mathbf{S}_i \end{bmatrix} \hat{\mathbf{t}}_h^{(j)} = - \begin{bmatrix} \mathbf{f}_{x,i} r^{(j)} \\ \mathbf{f}_{y,i} r^{(j)} \end{bmatrix} \\ \hat{\mathbf{t}}_h^{(j)} \geq \hat{\mathbf{t}}_{h,\min} \end{cases} \quad (11)$$

The objective function  $\sum_b \hat{\mathbf{t}}_h^{(b,j)}$  represents the sum of all components of  $\hat{\mathbf{t}}_h^{(j)}$ . Accordingly, the procedure searches for a solution  $\hat{\mathbf{t}}_h^{(j)}$  that closely approximates the assigned minimum values  $\hat{\mathbf{t}}_{h,\min}$ .

Using the reference thrusts  $\hat{\mathbf{t}}_h^{(j)}$  computed from the solution of Eq. (11), the  $x$  and  $y$  coordinates of the edge nodes can be calculated as:

$$\begin{aligned} \mathbf{x}_{i+e}^{(j)} &= - \left[ \mathbf{D}_{i+e}^{(j)} \right]^{-1} \left[ \mathbf{D}_{i+e}^{(j)} \mathbf{x}_r + \mathbf{f}_{x,i+e} r^{(j)} \right] \\ \mathbf{y}_{i+e}^{(j)} &= - \left[ \mathbf{D}_{i+e}^{(j)} \right]^{-1} \left[ \mathbf{D}_{i+e}^{(j)} \mathbf{y}_r + \mathbf{f}_{y,i+e} r^{(j)} \right] \end{aligned} \quad (12)$$

The described procedure has the potential to modify the positions of

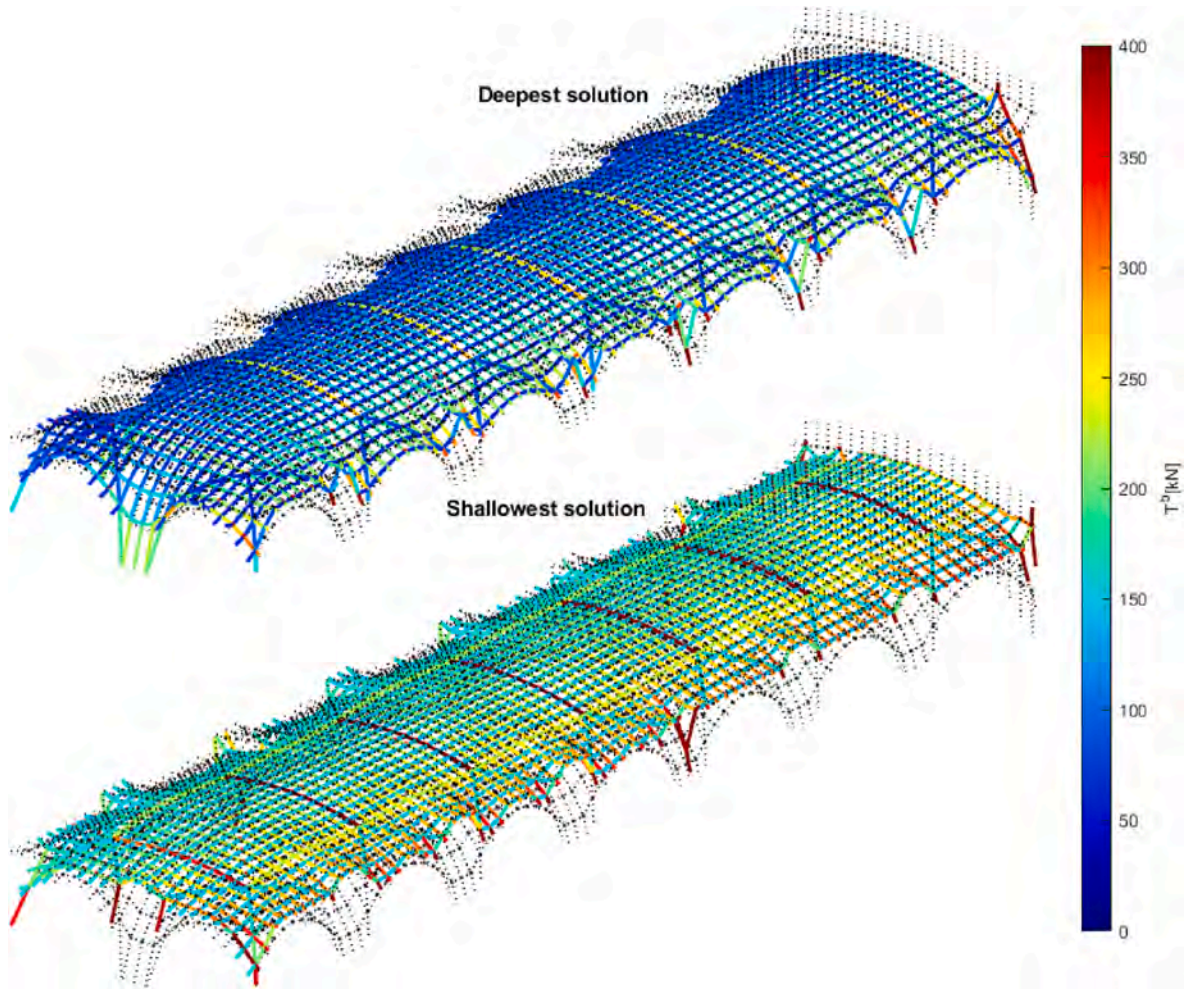


Fig. 20. Deepest and shallowest solutions for the vault subject to vertical and horizontal loads ( $\lambda = 0.59$ ,  $\alpha = 0$ ).

internal and edge nodes, contingent on the geometry and connectivity of the network. Typically, this effect on internal nodes is insignificant. However, if the application of Eq. (12) significantly changes their position, external loads must be recalculated.

After obtaining the  $j$ -th estimate of the horizontal position of all nodes, the nodal heights are computed, and a new estimate of  $r$  (i.e.,  $r_{j+1}$ ) is determined by solving the linearly constrained optimization problem expressed in Eq. (10) and relevant constraints. It reads:

$$\min_{\mathbf{z}, r} \pm r^{(j+1)} \text{ such that } \begin{cases} [\mathbf{D}_i^{(j)} \mathbf{f}_{z,i}] \begin{bmatrix} \mathbf{z}^{(j)} \\ r^{(j+1)} \end{bmatrix} = \mathbf{0}_i \\ \begin{bmatrix} \mathbf{z}_{\min} \\ 0 \end{bmatrix} \leq \begin{bmatrix} \mathbf{z}^{(j)} \\ r^{(j+1)} \end{bmatrix} \leq \begin{bmatrix} \mathbf{z}_{\max} \\ +\infty \end{bmatrix} \end{cases} \quad (13)$$

The lower and upper bounds of the nodal heights, denoted by  $\mathbf{z}_{\min}$  and  $\mathbf{z}_{\max}$  respectively, are specified by the designer. Typically, for internal nodes, these limits are established to match the heights of the vault's intrados and extrados. Alternatively, for complete compression of the vault section, they can be defined as the heights corresponding to the lower and upper thirds of the vault thickness.

To minimize  $r$  and obtain the shallowest network configuration, the objective function  $\pm r$  is set equal to  $+r$ . Conversely, to maximize  $r$  and obtain the deepest network configuration, the objective function is set to  $-r$ . Applying either one of these two objective functions one obtains either  $r_s$  or  $r_d$ , respectively. In both cases, the constraint  $0 \leq r \leq +\infty$  in (13) ensures that positive values of  $r$  are obtained.

The above described iterative procedure is terminated when two

successive estimates of  $r$  differ by a value lower than a given tolerance. In such a case, the solution is employed to evaluate the actual branch's thrusts as  $t^{(b)} = (\hat{\mathbf{t}}_h^{(b)} \ell^{(b)}) / (r \ell_h^{(b)})$ ,  $\ell^{(b)}$  being the  $b$ -th branch length.

#### 4.1.3. Specific solving procedure for the analysis of Turin cathedral central nave vaults

The vaults of the Turin Cathedral central nave have no openings or free edges; in such a case the solving procedure previously described can be simplified to increase computational performance. In such a case, the horizontal coordinates of all nodes of the thrust network are fixed and conditions in (11) are linear. Hence it is possible to express the generic solution  $\hat{\mathbf{t}}_h^{(j)}$  of (11) as

$$\hat{\mathbf{t}}_h^{(j)} = \hat{\mathbf{t}}_h^{(0)} + \frac{r^{(j)}}{r^{(1)}} [\hat{\mathbf{t}}_h^{(1)} - \hat{\mathbf{t}}_h^{(0)}] \quad \text{if } r^{(j)} \geq r^{(1)} \quad (14)$$

holding for any given value of  $r^{(j)}$ . In previous equation  $\hat{\mathbf{t}}_h^{(0)}$  and  $\hat{\mathbf{t}}_h^{(1)}$  are the reference thrusts obtained from the optimization procedure expressed in Eq. (11) with  $r = r^{(0)} = 0$  and  $r = r^{(1)} = r_1$ ,  $r_1$  being any positive scalar. It can be verified that (14) satisfies the constraints reported in Eq. (11) as long as  $r^{(j)} > r_1$ .

After evaluating  $\hat{\mathbf{t}}_h^{(0)}$  and  $\hat{\mathbf{t}}_h^{(1)}$ , the reference thrusts  $\hat{\mathbf{t}}_h^{(1)}$  are employed in Eq. (13) to estimate the heights of the nodes and retrieve a tentative value of  $r^{(2)}$ . This estimate of  $r$  is then utilized in Eq. (14) to calculate a new value of reference thrusts, which is again employed in Eq. (13) to retrieve a new estimation of the value of  $r$ . The procedure is reiterated until the solution converges.

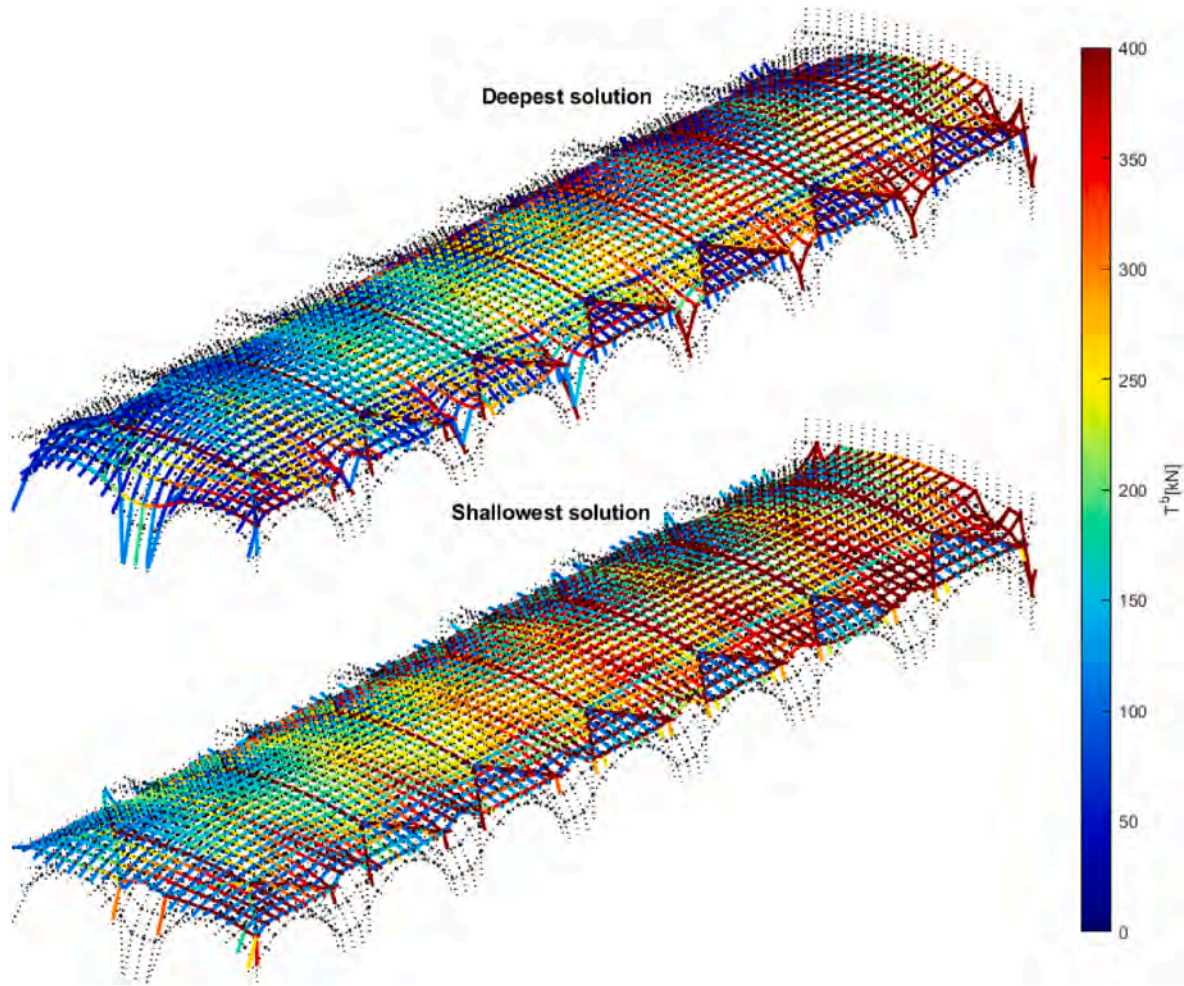


Fig. 21. Deepest and shallowest solutions for the vault subject to vertical and horizontal loads ( $\lambda = 1.56$ ,  $\alpha = \pi/8$ ).

#### 4.1.4. Limit conditions

Once the shallowest and deepest configurations of a thrust network are computed, the ratio between the two scaling parameters  $r_s$  and  $r_d$  can be employed to characterize the achievement of a limit condition for the vault. Considering all the admissible configurations, the ratio  $r_s/r_d$  represents the two extreme configurations: if  $r_s/r_d$  is equal to one, the shallowest and the deepest configurations of the thrust network are equal, defining the achievement of structural limit conditions. In this scenario, there is only one equilibrium solution represented by the thrust network falling within the geometric limits. The implication is that the structure has reached its ultimate limit strength.

In the case of low values of  $r_s/r_d$ , the shallowest and deepest configurations are very different, meaning that there are many possible structural solutions. In general, this condition characterizes safer structures.

The condition  $r_s/r_d = 1$  is generally adopted to define the limit loading condition or a geometrical extreme of the analyzed structure. This condition can be adopted to evaluate the geometric safety factor of the structure (Heyman, 1966). It involves establishing the limit multiplier for a specific loading condition or finding the minimum thickness necessary for equilibrium. For example, if the vault undergoes a combination of forces both in the horizontal and vertical directions, it is possible to determine the horizontal forces' maximum admissible multiplier by incrementally increasing its value until the ratio  $r_s/r_d = 1$ .

#### 4.2. TNA analysis of Turin's cathedral main nave vault

To determine the geometry of the vault of the central nave, an inspection was conducted in the Cathedral of Turin. During this phase, measurements were taken to precisely determine the geometries of the extrados and intrados of the vault.

This geometry is used to establish the thrust network node horizontal coordinates ( $x$  and  $y$ ). The limit heights of the thrust network model  $z_{\max}$  and  $z_{\min}$  are defined based on the measurement of the geometry of the extrados and intrados.

A grid located in the mid-surface of the central vault is adopted as the initial configuration to model the thrust network. The initial grid is characterized by a uniform horizontal spacing of  $0.44, m \times 0.44, m$ .

The initial configuration of the thrust network is a grid located on the mid-surface of the vault, characterized by a uniform horizontal spacing of  $0.44, m \times 0.44, m$ . To simulate thrusts along the groins of each *lunette*, diagonal additional branches have been included in the model. In Fig. 13, the initial configuration of the thrust network is presented, with the extrados and the intrados of the vault shaded in gray.

The structural self-weight is modelled as concentrated nodes applied on the nodes of the thrust network. The loads are calculated considering a weight per unit volume equal to  $18 \text{ kN/m}^3$ . As a result, a uniformly distributed load equal to  $5 \text{ kN/m}^2$  can be considered applied to the extrados of the vault. Finally, an additional load equal to  $61.5 \text{ kN}$  was considered to account for the concrete blocks and the fillings above the springers of the vault. This inclusion enables the analysis of the extra weights introduced by the restoration work carried out at the beginning

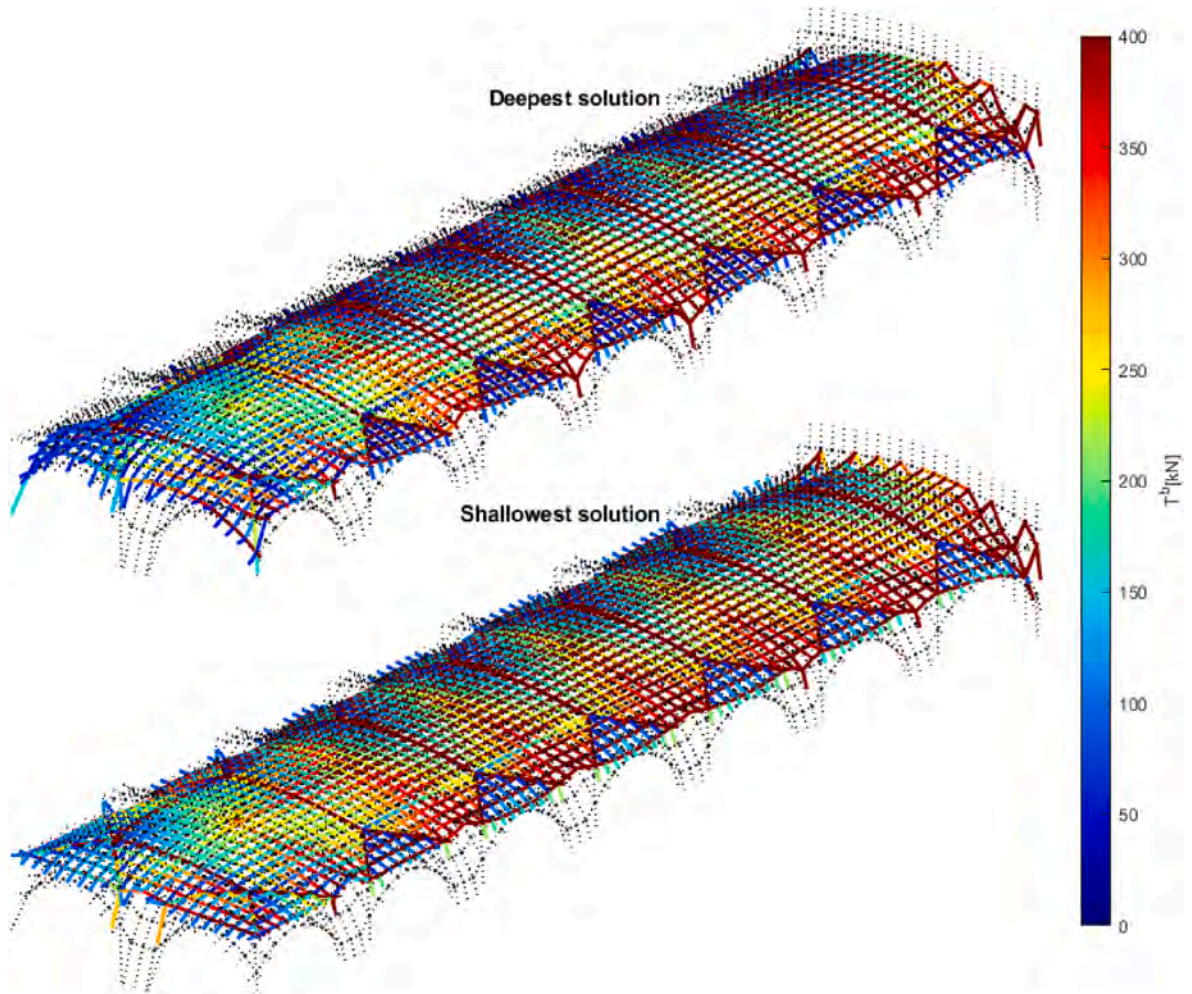


Fig. 22. Deepest and shallowest solutions for the vault subject to vertical and horizontal loads ( $\lambda = 2.06$ ,  $\alpha = \pi/4$ ).

of the 20th century.

Such a model has been used to both analyze the structure subjected to vertical loads only and to evaluate the minimum thickness of the vault by progressively reducing the vault thickness (modifying the heights of the extrados and the intrados) until reaching the limit condition  $r_s/r_d = 1$ . Additionally, such distribution of vertical loads has been applied in combination with horizontal loads to compute the horizontal loads limit multiplayer as a function of the direction of horizontal forces. This is done by assigning horizontal loads proportional to the vertical one, and progressively increasing their magnitude until reaching  $r_s/r_d = 1$ .

Both sets of results are described hereafter.

#### 4.2.1. The vault subjected to vertical loads only and the vault minimum thickness

Following the approach described in Section 4.1.4, the Thrust Network Analysis (TNA) has been employed to assess the vault minimum thickness. First, the vault has been analyzed by assuming its actual geometry and considering the effect of the vertical loads only. The shallowest and deepest configurations of the thrust network are shown in Fig. 14, where colour shades are used to represent thrust values in branches. As expected both solution are characterized by stress concentration at the extremities of lunettes, where the weight of concrete blocks and fillings bend downwards the thrust forces and provide a stabilizing vertical compression on the side walls.

Here it is clear how the two solutions are different both for the height of nodes and for the values of thrust in branches. This is confirmed by the relatively low value of  $r_s/r_d$ , which amounts to 0.78, meaning that the

two solutions are distinct one each other and the vault exhibits residual strength.

To evaluate the geometric safety factor of the vault subjected to vertical loads only, the thickness has been progressively reduced in order to reach the condition  $r_s/r_d = 1$ , denoting the attainment of the minimum thickness  $T_{\min}$ . Such a condition is met when the vault thickness is reduced to 63% of the actual thickness  $T$ . The corresponding network configurations are shown in Fig. 15. Notice how the two solutions are almost identical both in nodal height and thrust values, with negligible differences imputable to numerical round-off. Accordingly, the geometric safety factor of the vault amounts to  $T/T_{\min} = 1.59$ .

#### 4.2.2. The vault subjected to horizontal and vertical loads

The case of the vault subjected to the combined effect of both vertical and horizontal forces is considered by assigning horizontal forces as proportional to the vertical ones. The horizontal forces orientations were varied to assess the effect of different directions of the horizontal loading condition. Accordingly, the nodal forces' horizontal components are determined as  $f_x = \lambda |f_z| \cos(\alpha)$ ,  $f_y = \lambda |f_z| \sin(\alpha)$ . Here,  $\alpha$  denotes the angle between the horizontal action and the  $x$  axis of the global reference system (Fig. 13), while  $\lambda$  represents the multiplier of the horizontal load.

By leveraging the symmetry of the vault with respect to the longitudinal axis  $y$  of the nave, it is possible to reduce the number of significant loading scenarios. This reduction is achieved by considering nine distinct orientations of the horizontal loads. The variations are determined by adjusting the angle of the horizontal forces in increments of

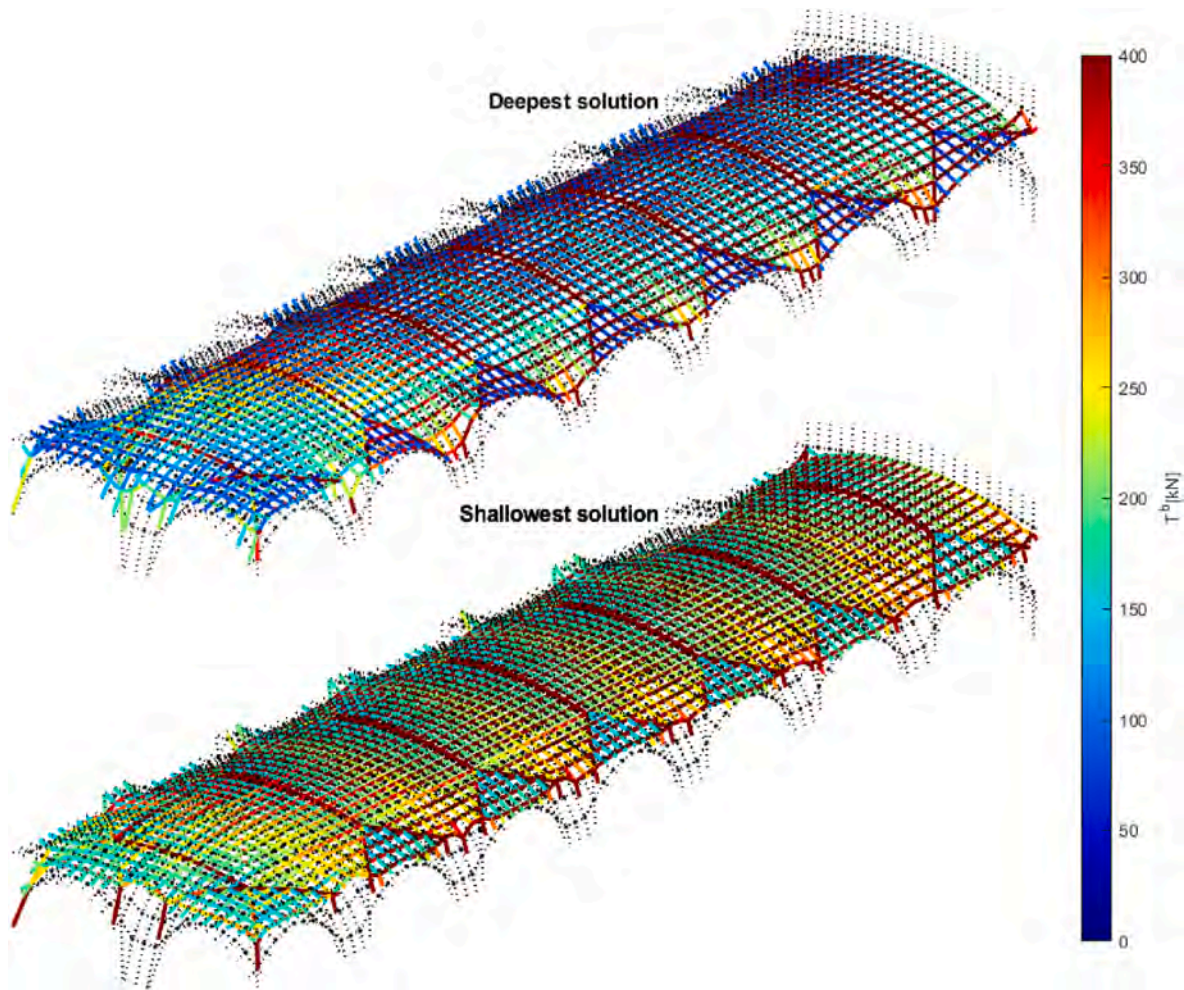


Fig. 23. Deepest and shallowest solutions for the vault subject to vertical and horizontal loads ( $\lambda = 1.39$ ,  $\alpha = 3\pi/8$ ).

$\pi/8$ . The range spans between  $\pi/2$ , which represents the forces towards the transept, and  $-\pi/2$ , which corresponds to the forces directed towards the narthex, parallel to the nave.

The corresponding solutions are reported in Figs. 16–24. Captions of all figures report the limit values of  $\lambda$  for each loading direction, above which the optimization solving procedure failed to reach convergence.

Fig. 16 shows that the vault is particularly vulnerable to horizontal forces acting at an angle  $\alpha = -\pi/2$ , i.e. towards the narthex since horizontal forces acting along this direction cannot exceed the limit value of 5.7% the vault self-weight. Actually, horizontal forces are here applied with a direction parallel to the Cathedral nave, towards the building facade and the lack of any buttressing structure capable of contrasting the vault thrust compromises the vault strength with respect to such loading conditions. Due to the very low value of horizontal forces, the thrust distribution within the thrust network is only slightly different from one computed for the vault subjected for vertical forces only. The main difference with respect to the case of no horizontal forces mainly regards the distribution of thrusts within the two lunettes near the church narthex.

In Figs. 17–19 the ratio between the component of the horizontal force acting towards the Cathedral facade and the transversal component decreases progressively. Consequently, the weakness of the facade influences less and less the structural performance. This is confirmed by the computed values of ultimate horizontal loads multipliers, which increase from the value of  $\lambda = 0.074$  when the direction of horizontal forces is  $\alpha = -3\pi/8$  (Fig. 17), to  $\lambda = 0.094$  when  $\alpha = -\pi/4$  (Fig. 18), reaching the value of  $\lambda = 0.105$  when  $\alpha = -\pi/8$  (Fig. 19). The

corresponding thrust distribution shows higher values on lunettes on the right-hand side of the vault, which is the portion of the structure towards which horizontal forces are acting.

Fig. 20 refers to horizontal forces acting in the direction perpendicular to the nave longitudinal axis ( $\alpha = 0$ ). In this case,  $\lambda$  reaches the value  $\lambda = 0.59$ . Except for the region next to the two narthex lunettes, the distribution of thrusts throughout the vault longitudinal axis is roughly uniform. In the transversal direction, higher values of thrusts are computed on the right-hand side of the vault, i.e. the side receiving the horizontal forces.

Figs. 21–23 refer to the case of horizontal forces that have a higher and higher component towards the church transept. In these cases the limit values of  $\lambda$  reach the values of 1.56 when  $\alpha = \pi/8$  (Fig. 21), and 2.06 when  $\alpha = \pi/4$  (Fig. 22). Singularly  $\lambda$  decreases to 1.39 when  $\alpha = 3\pi/8$ . Thrust distributions show a strong variability of values across the vault, with higher values clustering in the areas between side lunettes. In the cases,  $\alpha = \pi/8$  and  $\alpha = \pi/4$ , thrust network configurations become almost horizontal on the right-hand-side of the vault, both for the deepest and shallowest solutions, while the left-hand side of the deepest configurations follow the geometry of lunettes on this side of the nave. The behaviour of the vault subjected to horizontal forces acting with an angle  $\alpha = 3\pi/8$  is slightly different. Actually, differently from the other two cases, the deepest configuration follows the lunettes geometry on the right-hand side of the vault, and it becomes almost horizontal on the left narthex lunette. This shows that the reduction of the horizontal load multiplier computed for this last case is probably due to the weakening effect produced by the presence of the frontal lunettes.

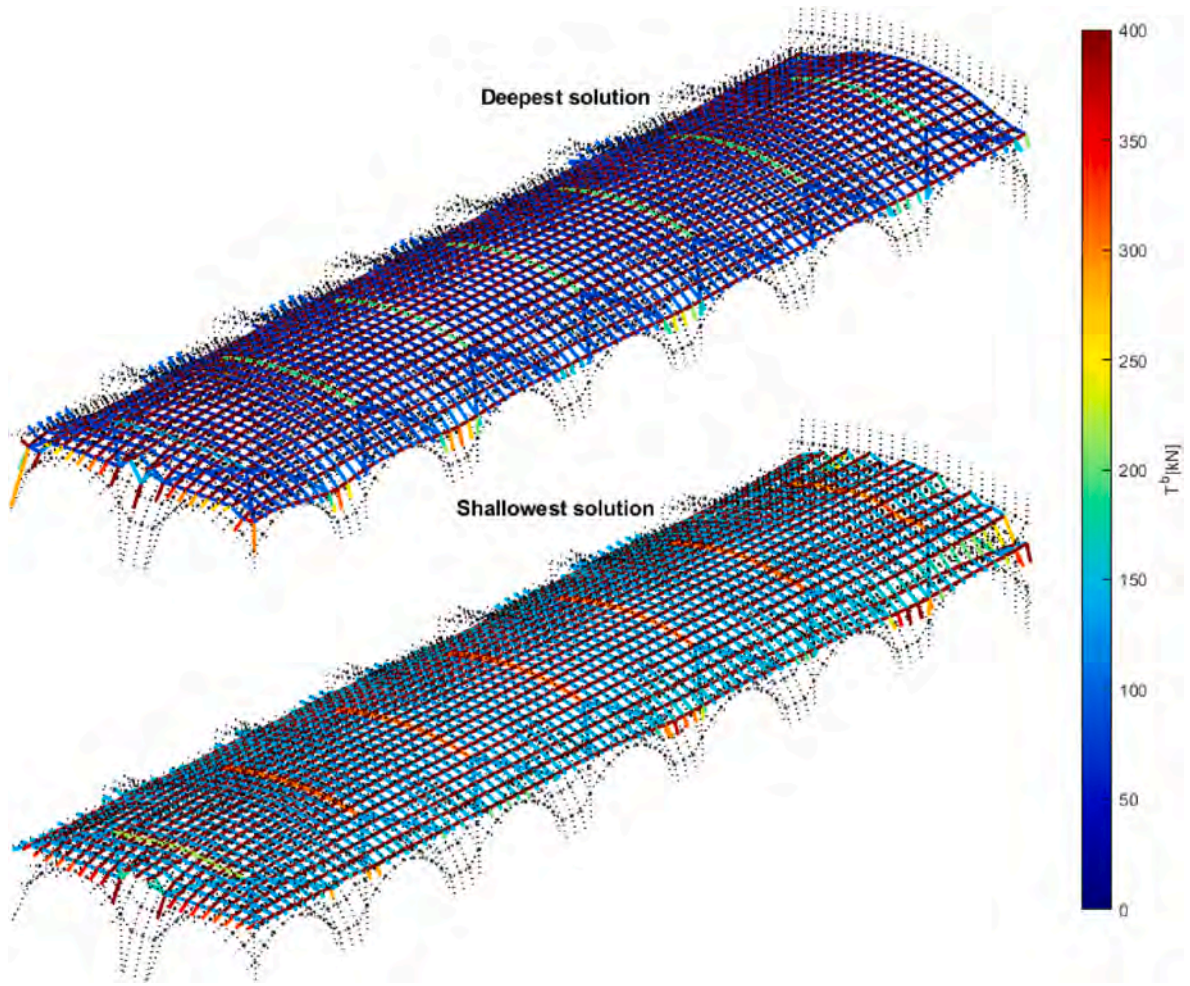


Fig. 24. Deepest and shallowest solutions for the vault subject to vertical and horizontal loads ( $\lambda = 12.22$ ,  $\alpha = \pi/2$ ).

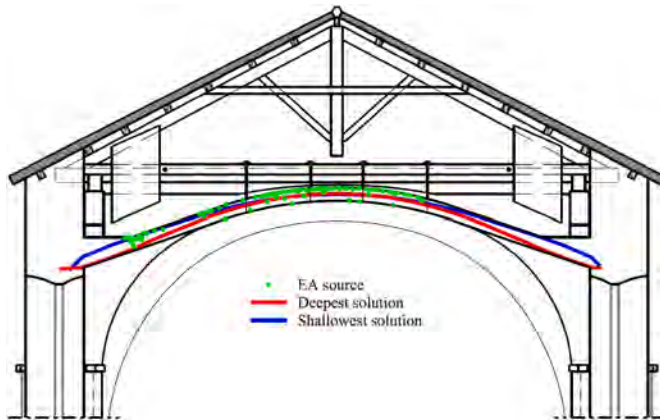


Fig. 25. Deepest and shallowest solutions for the vault subject to vertical loads and position of AE sources.

Finally, Fig. 24 refers to the case in which horizontal forces are acting parallel to the nave longitudinal axis, towards the transept. The vault is visibly stronger when subjected to such a loading condition and  $\lambda$  reaches the remarkable value of 12.22, which must be considered as a mere theoretical limit. In this last case, the narthex lunettes are substantially unloaded, while the main barrel vault is loaded longitudinally. Transverse thrusts are very low, while longitudinal branches of the thrust network experience very high values of thrust since these are parallel to

the direction of horizontal loads and are responsible for their transmission towards the church transept.

Fig. 25 shows the deepest and shallowest solutions for the vault subject to vertical loads and the results of the localization procedures performed by the i-AIC method. The results appear particularly interesting considering that most of the sources of the localized signals coincide with the shallowest solution. In addition, on the side of the section, it is also evident the presence of a cluster of AE sources at the connection between the left lunette and the extrados of the vault. The findings shown in Fig. 25 can be utilized to obtain some understanding of the true internal forces distribution within the vault as well as to validate the results of the numerical study. Cracks are confined above the vault mid-surface because AE sources are mostly concentrated at the vault extrados. The distribution of fractures, which may be attributed to tensile stresses, is consistent with the thrust network's deepest design, which exhibits compression forces at the vault intrados, particularly in the vicinity of the two vault sides. This finding is consistent with the concept of least action, which states that the minimal value of horizontal thrust—that is, the deepest arrangement of the masonry arches and vaults—corresponds to the actual internal thrust distribution.

## 5. Conclusions

AE monitoring parameters of the Turin Cathedral's central nave is presented in this article. Utilizing the AE technique, eight distinct piezoelectric sensors were installed in order to conduct the structural monitoring and to recognize the evolving damage. The equipment that was installed made possible the acquisition of the main indexes of the AE

signals emitted during the crack propagation inside the vault. Next, the improved AIC picker technique was used to determine the AE signals onset time and, subsequently, the localization of AE sources.

Moreover, the thrust network analysis method was employed to model the structure and identify the load paths within the vaults. The TNA was utilized to assess both the minimum thickness of the vault and its geometric safety factor, which amounts to about 1.6 when the vault is subjected to vertical loads only. The deepest and shallowest configurations of the thrust network, see, e.g., Fig. 14, can be put in relation with the location of AE sources, see, e.g., Fig. 11a) and b). The most significant comparison can be done by comparing the position of AE sources and the geometry of the deepest and shallowest solutions of the TNA as shown on the vault transversal section of Fig. 25, and can be used both as a validation of the numerical analysis results and to gain some insight about the actual internal forces distribution within the vault. AE sources are mostly localized at the vault extrados, meaning that cracks are localized above the vault mid-surface. This distribution of cracks, which is likely imputable to tensile strains, is compatible with the deepest configuration of the thrust network which, especially near the two sides of the vault, shows compression forces at the vault intrados. This observation agrees with the principle of least action, which implies that the actual internal thrust distribution in masonry arches and vaults is the one that corresponds to the minimum value of horizontal thrust, namely the deepest configuration of the thrust line or network.

Additional analyses of the vault equilibrium have been conducted with the goal of determining the vault strength with respect to horizontal loads. To this end, horizontal forces have been applied with a variable angle of application with respect to the vault's longitudinal axis. Vault resistance against horizontal forces is the minimum when forces are directed towards the church narthex, probably due to the presence of two lunettes on the back of the building facade. The vault strength increases progressively as the orientation of horizontal forces is rotated becoming first transversal with respect to the vault longitudinal axis and finally directed towards the church transept. It is worth noting that, as horizontal seismic forces are proportional to the structural weight, the additional mass introduced by the presence of concrete blocks is undesirable. However, on the other hand, the weight of these blocks has a stabilizing effect on the structure. This contribution enhances the overall balance, particularly when the structure is primarily subjected to vertical loads, as it introduces additional vertical compression on the side walls.

Finally, this research proposes an integration between the Acoustic Emissions (AE) and Thrust Network Analysis (TNA) for the stability assessment of the central nave vaults of the Turin Cathedral. The proposed approach is general and can be applied to general masonry vaults: AE monitoring can be used to evaluate the vault structural integrity by locating and identifying cracks thanks to the application of piezoelectric sensors and the upgraded AIC picker technique; TNA can give insights into the load paths inside the vault and allows identifying limit equilibrium conditions for the structure in presence of both vertical and horizontal loading conditions. The combination of these two methods, one experimental, and the other numerical, is capable of increasing the comprehension of the structural behaviour and the preservation requirements of old masonry constructions.

#### CRedit authorship contribution statement

**Amedeo Manuello:** Writing – original draft, Validation, Supervision, Resources, Project administration, Methodology, Investigation, Formal analysis, Data curation, Conceptualization. **Francesco Marmo:** Writing – review & editing, Writing – original draft, Validation, Supervision, Resources, Methodology, Investigation, Formal analysis, Data curation, Conceptualization. **Jonathan Melchiorre:** Writing – review & editing, Writing – original draft, Investigation, Formal analysis.

#### Declaration of competing interest

The authors declare that they have no known competing financial interests or personal relationships that could have appeared to influence the work reported in this paper.

#### Data availability

Data will be made available on request.

#### References

- Aggelis, D., Mpalaskas, A., Matikas, T., 2013. Investigation of different fracture modes in cement-based materials by acoustic emission. *Cement Concr. Res.* 48, 1–8.
- Aki, K., 1981. A probabilistic synthesis of precursory phenomena, *Earthquake prediction: an. Int. Rev.* 4, 566–574.
- Anant, K.S., Dowla, F.U., 1997. Wavelet transform methods for phase identification in three-component seismograms. *Bull. Seismol. Soc. Am.* 86 (6), 1598–1612.
- Angelillo, M., Fortunato, A., 2004. Equilibrium of masonry vaults. In: *Novel Approaches in Civil Engineering*. Springer, pp. 105–111.
- Angelillo, M., Cardamone, L., Fortunato, A., 2010. A numerical model for masonry-like structures. *J. Mech. Mater. Struct.* 5 (4), 583–615.
- Anzani, A., Binda, L., Carpinteri, A., Lacidogna, G., Manuello, A., 2008. Evaluation of the repair on multiple leaf stone masonry by acoustic emission. *Mater. Struct.* 41, 1169–1189.
- Bak, P., Tang, C., 1989. Earthquakes as a self-organized critical phenomenon. *J. Geophys. Res. Solid Earth* 94 (B11), 15635–15637.
- Bak, P., Christensen, K., Danon, L., Scanlon, T., 2002. Unified scaling law for earthquakes, 88 (17), 178501.
- Block, P.P.C.V., 2009. Thrust Network Analysis: Exploring Three-Dimensional Equilibrium. Massachusetts Institute of Technology. Ph.D. thesis.
- Block, P., Lachauer, L., 2014. Three-dimensional (3d) equilibrium analysis of Gothic masonry vaults. *Int. J. Architect. Herit.* 8 (3), 312–335.
- Block, P., Ochsendorf, J., 2007. Thrust network analysis: a new methodology for three-dimensional equilibrium. *Journal of the International Association for shell and spatial structures* 48 (3), 167–173.
- Carpinteri, A., Xu, J., Lacidogna, G., Manuello, A., 2012. Reliable onset time determination and source location of acoustic emissions in concrete structures. *Cement Concr. Compos.* 34 (4), 529–537.
- Carpinteri, A., Lacidogna, G., Invernizzi, S., Manuello Bertetti, A., et al., 2013a. Ae monitoring and structural modeling of the asinelli tower in bologna. In: *Proceedings of the 13th International Conference on Fracture (ICF13)*, China Science Literature. Publishing House, p. 234.
- Carpinteri, A., Lacidogna, G., Accornero, F., Mpalaskas, A., Matikas, T., Aggelis, D., 2013b. Influence of damage in the acoustic emission parameters. *Cement Concr. Compos.* 44, 9–16.
- Carpinteri, A., Lacidogna, G., Manuello, A., Niccolini, G., 2016. A study on the structural stability of the asinelli tower in bologna. *Struct. Control Health Monit.* 23 (4), 659–667.
- Earle, P., Shearer, P.M., 1994. Characterization of global seismograms using an automatic-picking algorithm. *Bull. Seismol. Soc. Am.* 84 (2), 366–376.
- Fraddosio, A., Lepore, N., Piccioni, M.D., 2020. Thrust surface method: an innovative approach for the three-dimensional lower bound limit analysis of masonry vaults. *Eng. Struct.* 202, 109846.
- Fraternali, F., 2010. A thrust network approach to the equilibrium problem of unreinforced masonry vaults via polyhedral stress functions. *Mech. Res. Commun.* 37 (2), 198–204.
- Gáspár, O., Sipos, A.A., Sajtos, I., 2018. Effect of stereotomy on the lower bound value of minimum thickness of semi-circular masonry arches. *Int. J. Architect. Herit.* 12 (6), 899–921.
- Heyman, J., 1966. The stone skeleton. *Int. J. Solid Struct.* 2 (2), 249–279.
- Heyman, J., 1967. On shell solutions for masonry domes. *Int. J. Solid Struct.* 3 (2), 227–241.
- Huerta, S., 2006. Galileo was wrong: the geometrical design of masonry arches. *Nexus Netw. J.* 8, 25–52.
- Lacidogna, G., Manuello, A., Niccolini, G., Carpinteri, A., 2015. Acoustic emission monitoring of Italian historical buildings and the case study of the athena temple in syracuse. *Architect. Sci. Rev.* 58 (4), 290–299.
- Lenticchia, E., Manuello, A., Ceravolo, R., 2021. Ae propagation velocity calculation for stiffness estimation in pier luigi nervi's concrete structures. *Curved Layer. Struct.* 8 (1), 109–118.
- Li, Z., Shah, S.P., 1994. Localization of microcracking in concrete under uniaxial tension. *Materials Journal* 91 (4), 372–381.
- Manuello, A., Masera, D., Alberto, C., 2020. Reformulation and extension of the thrust network analysis. *Appl. Sci.* 10, 3931.
- Marmo, F., Rosati, L., 2017. Reformulation and extension of the thrust network analysis. *Comput. Struct.* 182, 104–118.
- Marmo, F., Masi, D., Rosati, L., 2018a. Thrust network analysis of masonry helical staircases. *Int. J. Architect. Herit.* 12 (5), 828–848.
- Marmo, F., Ruggieri, N., Toraldo, F., Rosati, L., 2018b. Historical study and static assessment of an innovative vaulting technique of the 19th century. *Int. J. Architect. Herit.*

- Melchiorre, J., Manuello Bertetto, A., Rosso, M.M., Marano, G.C., 2023a. Acoustic emission and artificial intelligence procedure for crack source localization. *Sensors* 23 (2), 693.
- Melchiorre, J., Rosso, M.M., Cucuzza, R., D'Alto, E., Manuello, A., Marano, G.C., 2023b. Deep acoustic emission detection trained on seismic signals. In: *Applications of Artificial Intelligence and Neural Systems to Data Science*. Springer, pp. 83–92.
- Niccolini, G., Bosia, F., Carpinteri, A., Lacidogna, G., Manuello, A., Pugno, N., 2009. Self-similarity of waiting times in fracture systems. *Phys. Rev.* 80 (2), 026101.
- Niccolini, G., Carpinteri, A., Lacidogna, G., Manuello, A., 2011a. Acoustic emission monitoring of the syracuse athena temple: scale invariance in the timing of ruptures. *Phys. Rev. Lett.* 106 (10), 108503.
- Niccolini, G., Carpinteri, A., Lacidogna, G., Manuello, A., 2011b. Acoustic emission monitoring of the syracuse athena temple: scale invariance in the timing of ruptures. *Phys. Rev. Lett.* 106 (10), 108503.
- Ohtsu, M., Okamoto, T., Yuyama, S., 1998. Moment tensor analysis of acoustic emission for cracking mechanisms in concrete. *Structural Journal* 95 (2), 87–95.
- O'Dwyer, D., 1999. Funicular analysis of masonry vaults. *Comput. Struct.* 73 (1–5), 187–197.
- Q, H., J, X., A, C., G, L., 2015. Localization of acoustic emission sources in structural health monitoring of masonry bridge. *Struct. Control Health Monit.* 22 (3), 314–329.
- Scruby, C.B., 1987. An introduction to acoustic emission. *J. Phys. E Sci. Instrum.* 20 (8), 946.
- Sleeman, R., Van Eck, T., 1999. Robust automatic p-phase picking: an on-line implementation in the analysis of broadband seismogram recordings. *Phys. Earth Planet. In.* 113 (1–4), 265–275.
- Tong, C., Kennet, B., 1996. Automatic seismic event recognition and later phase identification for broadband seismograms. *Bull. Seismol. Soc. Am.* 86 (6), 1896–1909.
- Tralli, A., Alessandri, C., Milani, G., et al., 2014. Computational methods for masonry vaults: a review of recent results. *Open Civ. Eng. J.* 8 (Special Issue# 2), 272–287.
- Withers, M., et al., 1998. A comparison of select trigger algorithms for automated global seismic phase and event location. *Bull. Seismol. Soc. Am.* 81 (1), 95–106.